HHS Public Access

Author manuscript

Eng Anal Bound Elem. Author manuscript; available in PMC 2022 July 01.

Published in final edited form as:

Eng Anal Bound Elem. 2021 July 1; 128: 274–289. doi:10.1016/j.enganabound.2021.04.006.

An arbitrary Lagrangian Eulerian smoothed particle hydrodynamics (ALE-SPH) method with a boundary volume fraction formulation for fluid-structure interaction

Bruno Jacob[#a], **Brian Drawert**[#b], **Tau-Mu Yi**[c], **Linda Petzold**[a,d]

[a]Department of Mechanical Engineering, University of California-Santa Barbara, Santa Barbara, California, 93106, USA

[b]Department of Computer Science, University of North Carolina at Asheville, Asheville, North Carolina, 28804, USA

[c]Department of Molecular, Cellular, and Developmental Biology, University of California-Santa Barbara, Santa Barbara, California 93106, USA

[d]Department of Computer Science, University of California-Santa Barbara, Santa Barbara, California, 93106, USA

[#] These authors contributed equally to this work.

Abstract

We present a new weakly-compressible smoothed particle hydrodynamics (SPH) method capable of modeling non-slip fixed and moving wall boundary conditions. The formulation combines a boundary volume fraction (BVF) wall approach with the transport-velocity SPH method. The resulting method, named SPH-BVF, offers detection of arbitrarily shaped solid walls on-the-fly, with small computational overhead due to its local formulation. This simple framework is capable of solving problems that are difficult or infeasible for standard SPH, namely flows subject to large shear stresses or at moderate Reynolds numbers, and mass transfer in deformable boundaries. In addition, the method extends the transport-velocity formulation to reaction-diffusion transport of mass in Newtonian fluids and linear elastic solids, which is common in biological structures. Taken together, the SPH-BVF method provides a good balance of simplicity and versatility, while avoiding some of the standard obstacles associated with SPH: particle penetration at the boundaries, tension instabilities and anisotropic particle alignments, that hamper SPH from being applied to complex problems such as fluid-structure interaction in a biological system.

Keywords

Solid wall model; Transport-velocity; Smoothed particle hydrodynamics; Boundary condition; Deforming boundaries

[*]Corresponding author bruno@engineering.ucsb.edu (Bruno Jacob).

1. Introduction

Smoothed particle hydrodynamics (SPH) is a meshless particle method based on a Lagrangian formulation [1], proposed independently by Gingold and Monaghan [2] and Lucy [3] as a method to simulate astrophysical problems. Since its development, SPH has been used in a wide range of applications, including colloidal suspensions [4, 5], nanofluidics [6], blood flow [7, 8], multiphase flows [9], polymer chains [10] and red blood cell deformations [11].

In contrast to grid-based methods, SPH uses a kernel estimation at Lagrangian points (particles) to approximate the partial differential equations (PDEs) that govern the system of interest. When compared with standard mesh-based methods,such as finite element (FEM), finite difference (FDM) and finite volume (FVM), SPH offers attractive advantages. As a consequence of its Lagrangian description, advection is treated exactly, allowing the simulation of arbitrary free-shear flow in systems with complex geometries without the need to use an adaptive mesh or interface tracking [12, 13]. Another important feature of the method is its inherent adaptivity, as particle attributes evolve according to their material time derivative [14]. More recently, the development of multi-resolution SPH brings the method closer to industrial applications by adaptively increasing the resolution by means of splitting particles in regions of interest, and coalescing particles in regions where lower resolutions suffices [15, 16, 17, 18, 19].

Despite all of these advantages, the treatment of solid wall boundaries in SPH remains a challenge. Recent studies [20, 21, 22, 23, 24, 25, 26, 27, 28, 29, 30] have demonstrated that despite several improvements, the development of a robust, efficient and accurate method capable of preventing particle penetration under no-slip and partial-slip conditions remains an open problem. In fact, some consider it to be one of the grand challenges for the advancement of SPH [31].

The work of Valizadeh and Monaghan [32] provides a comprehensive review of the available solid wall models, comparing the performance of the most widely-used strategies and highlighting their capabilities and drawbacks. They classify the different models of solid boundaries into three main groups: (i) semi-analytical, (ii) ghost particles and (iii) boundary force methods. In the semi-analytical approach [25], surface integrals must be approximated using the SPH formalism. A limitation of this class of methods is the complexity of the algorithm, as many modifications are necessary to help prevent particle penetration on the solid boundary. In the ghost particles approach [33], a set of fictitious particles are created in the wall in order to guarantee non-slip and prevent penetration. Despite being conceptually attractive, the treatment of complex geometries is not straightforward. Similarly challenging, the computational algorithm typically requires the creation/destruction of particles at specific wall positions at each time step, causing memory access overheads and additional communication in otherwise parallel tasks.

These limitations make the class of boundary force methods a simple and attractive alternative. As a common feature, these methods use predetermined layers of particles to

model boundaries. The variants in this class differ in the way velocity and density are communicated between wall and fluid particles. For example, in the method developed by Monaghan and Kajtar [23], a Lennard-Jones boundary force is added to the momentum equation for particles in the neighborhood of the walls, in a similar manner as the forces used in the immersed boundary method [34]. This approach, despite its simplicity, is effective for a wide range of problems, provided that all the parameters of the boundary force are calibrated correctly.

In the work of Adami et al. [22], the pressure and velocity of boundary particles are computed using interpolation of the fluid field, thus implicitly enforcing the impermeability condition of rigid walls. Unlike the method of Monaghan and Kajtar [23], this method does not require parameter calibration. In fact, the detailed study of Valizadeh and Monaghan [32] concluded that the method of Adami et al. [22] is overall the best method available. More recently, Khayyer et al. [35] obtained good results for an enhanced incompressible SPH method and a pressure-based, physically-derived boundary condition. Similarly, Zhan et al. [36] obtained excellent results and nearly quadratic convergence by using stabilization techniques to achieve higher accuracy. However, both frameworks used the boundary condition proposed by Adami et al. [22] in which there is no mathematical guarantee that particle penetration is prevented.

Recently a new method, designed primarily for dissipative particle dynamics (DPD) systems, was proposed by Li et al. [37]. This method introduces an indicator variable, which measures the boundary volume fraction (BVF) of particles near solid walls, and employs a predictor-corrector integration to prevent particle penetration. As a result, the fluid particles become autonomous to find wall surfaces in arbitrarily shaped objects, based solely on the coordinates of their neighboring particles. Thus, this method prevents particle penetration with minimal computational overhead by using a local formulation.

In this context we propose a new SPH formulation combining the BVF wall treatment with the transport-velocity discretization. The resulting method, named SPH-BVF, is versatile, accurate and allows the modeling of fixed and moving boundaries. In contrast to the method proposed by Adami et al. [22], the impermeability is explicitly enforced during the time integration, and no further correction of the pressure field is required. Furthermore, we improve the BVF method for the case of moving boundaries by using weighted interpolations of the solid particles to determine the wall velocity and accelerations, resulting in an algorithm capable of dealing with deforming boundaries. Finally, we introduce the reaction-diffusion equation in our formulation, extending the usage of the method to conjugate mass transport problems in moving boundaries, enabling simulations where boundary deformations are caused by reaction-diffusion events. This step is crucial in enabling SPH to simulate certain biological systems in which enzymatic reactions trigger processes that modify the boundary properties.

The main features of the SPH-BVF method include (a) algorithmic simplicity; (b) retaining the locality and intrinsic parallelism of the SPH method at the cost of a small overhead; (c) preventing the three major problems in standard SPH methods: particle penetration at the boundaries, tension instabilities and anisotropic structures. We demonstrate these

capabilities and validate the proposed method using canonical examples and compare the results with the literature. Finally, we test the new method on a biomechanical cell wall polarization problem that incorporates multiple physics (species transport, solid and fluid mechanics), and thus could not be solved by existing SPH methods and remains challenging for advanced commercial multiphysics FEM tools.

This paper is organized as follows: Section 2 briefly describes the transport-velocity SPH formulation. Section 3 provides the additional equations required for the SPH-BVF method and its algorithm. Sections 4 and 5 present validations, applications, and discussion of relevant results. Finally, conclusions and future perspectives are discussed in Section 6.

2. SPH formulation

In this section we provide a brief overview of the governing equations, the SPH discretizations and the temporal integration method proposed.

2.1. Governing equations and transport-velocity formulation

The continuum mechanics equations for the conservation of mass, linear momentum and concentration of species in a Lagrangian reference frame are given by

$$\frac{d\rho}{dt} = -\rho\nabla\cdot\boldsymbol{v}, \tag{1}$$

$$\frac{d\boldsymbol{v}}{dt} = \frac{1}{\rho}\nabla\cdot\boldsymbol{\sigma} + \boldsymbol{F}_{\mathrm{B}}, \tag{2}$$

$$\frac{dC}{dt} = \nabla\cdot(\alpha\nabla C) + R, \tag{3}$$

where ρ, $\boldsymbol{v}$, $\boldsymbol{\sigma}$, $\boldsymbol{F}_{\mathrm{B}}$, C, α and R denote the fluid density, velocity, Cauchy stress tensor, body force, concentration, mass diffusivity and reaction term, respectively. The $d(\cdot)/dt$ operator denotes the material derivative [38].

One of the most relevant problems of standard, purely Lagrangian SPH discretizations of Eqs. (1)-(3) is the onset of anisotropic particle structures formed as the particles follow the Lagrangian trajectories. This problem was first addressed by Nestor et al. [39] by introducing the concept of particle shifting, where a small perturbation is inserted to the particle trajectories, reducing the formation of anisotropic structures. Later, the work of Shadloo et al. [40] applied particle shifting to a weakly compressible SPH formulation, obtaining improved results in fluid flow problems. More recent improvements include the usage of particle shifting in free surface flows for incompressible SPH formulations [41], and stabilized particle shifting techniques [42]. Oger et al. [43] clarified that this issue is particularly relevant in fluid flows in which there is a natural tendency of particle alignment, such as flows subject to stretching and shear stresses. A similarly relevant problem is the so-called tensile instability, a phenomenon that causes particles to clump when subject to a tension stress state [44], being particularly relevant in fluid-structure interactions, solids

under large deformations and flows under high Reynolds numbers. Incidentally, both of these limiting issues are alleviated by using the transport-velocity formulation, proposed by Adami et al. [22] for fluids and later extended to solid mechanics by Zhang et al. [45]. The transport-velocity formulation consists of a particular type of Arbitrary Lagrangian Eulerian (ALE) formalism [43], where particles are advected by an arbitrary transport velocity, specifically tuned so that the pressure field is kept positive, thus avoiding the tensile instability, while at the same time it causes a small shift in the particle trajectories, avoiding the formation of coherent structures of particles. For a detailed numerical analysis of the transport-velocity SPH formulation, we refer the reader to Litvinov et al. [46].

The transport-velocity equations are obtained by rewriting the material derivative operator for a particle moving with a modified advection velocity $\tilde{\boldsymbol{v}}$ as

$$\frac{\tilde{d}(\bullet)}{dt} = \frac{\partial(\bullet)}{\partial t} + \tilde{\boldsymbol{v}} \cdot \boldsymbol{\nabla}(\bullet)\,. \tag{4}$$

The presence of the modified transport velocity, $\tilde{\boldsymbol{v}}$, modifies the material derivative operator with two relative velocity terms, leading to the following identity

$$\frac{d(\bullet)}{dt} = \frac{\tilde{d}(\bullet)}{dt} + \boldsymbol{\nabla} \cdot [(\bullet)(\boldsymbol{v} - \tilde{\boldsymbol{v}})] - (\bullet)\boldsymbol{\nabla} \cdot (\boldsymbol{v} - \tilde{\boldsymbol{v}}), \tag{5}$$

where, due to the weakly compressible approximation [12, 45], it is safe to assume that $\boldsymbol{\nabla} \cdot (\boldsymbol{v} - \tilde{\boldsymbol{v}}) \approx 0$. Thus, the transport-velocity formulation of the conservation laws, Eqs. (1)-(3), yields

$$\frac{\tilde{d}\rho}{dt} = -\rho\boldsymbol{\nabla} \cdot \boldsymbol{v} - \boldsymbol{\nabla} \cdot [\rho(\boldsymbol{v} - \tilde{\boldsymbol{v}})], \tag{6}$$

$$\frac{\tilde{d}\boldsymbol{v}}{dt} = \frac{1}{\rho}\boldsymbol{\nabla}\boldsymbol{\sigma} + \boldsymbol{F}_{\mathrm{B}} - \boldsymbol{\nabla} \cdot [\boldsymbol{v}(\boldsymbol{v} - \tilde{\boldsymbol{v}})], \tag{7}$$

$$\frac{\tilde{d}C}{dt} = \boldsymbol{\nabla} \cdot (\alpha\boldsymbol{\nabla}C) + R - \boldsymbol{\nabla} \cdot [C(\boldsymbol{v} - \tilde{\boldsymbol{v}})]\,. \tag{8}$$

Equations (6)-(8) form the set of governing equations of the SPH-BVF formulation. Additional conservation laws can be added as needed, using the identity provided by Eq. (5). Notice that this formulation can be seen as a generic version of SPH schemes for an arbitrary reference frame [43], where $\tilde{\boldsymbol{v}}$ is the referential velocity. For instance, if $\tilde{\boldsymbol{v}} = \boldsymbol{v}$, Eqs. (6)-(8) reduce to the classical, purely Lagrangian formulation. In contrast, setting $\tilde{\boldsymbol{v}} = 0$ results in a formulation for an inertial (Eulerian) reference frame. In the following sections, we discuss the usage of $\tilde{\boldsymbol{v}}$ and how this term is discretized.

2.2. SPH discretization

In SPH, the mapping between the primitive variables (mass, momentum and concentrations) and the discrete particle system is done using two different approximations: a radial basis function kernel interpolation and a quadrature approximation. The radial basis function kernel interpolation consists of approximating a continuous function $f:\mathbb{R}^3 \mapsto \mathbb{R}$, defined at coordinates $\boldsymbol{x}$ in $\Omega \subseteq \mathbb{R}^3$, by the integral equation with a smoothing kernel function W with compact support h

$$f(\boldsymbol{x}) \approx \int_{\Omega} f(\boldsymbol{x}')W(\boldsymbol{x}-\boldsymbol{x}', h)d\boldsymbol{x}' . \tag{9}$$

The accuracy of the approximation in Eq. (9) depends on the choice of W. For the sake of simplicity, we have adopted in this work the Lucy kernel, proposed by Lucy [3], with $\boldsymbol{x}_{ij} = \boldsymbol{x} - \boldsymbol{x}'$ and $\xi = \|\boldsymbol{x}_{ij}\|_2/h$ denoting a generalized coordinate

$$W(\xi) = \begin{cases} \alpha_D (1+3\xi)(1-\xi)^3, & \text{if } 0 \le \xi \le 1, \\ 0, & \text{otherwise,} \end{cases} \tag{10}$$

and the spatial derivative

$$\nabla W = \frac{\boldsymbol{x}}{x}\frac{dW}{d\xi}, \tag{11}$$

where the normalization parameter α_D depends on the dimensionality of the problem:

$$\alpha_D = \begin{cases} 5/4h, & \text{if 1D,} \\ 5/\pi h^2, & \text{if 2D,} \\ 105/16\pi h^3, & \text{if 3D .} \end{cases} \tag{12}$$

For details on choosing W, the reader may refer to the work of Xu and Deng [13]. The second approximation consists of rewriting the integral given by Eq. (9) as a discrete sum. The domain Ω is then discretized using N particles, each located at coordinates $\boldsymbol{x}_i$. The kernel approximations of f and ∇f are given by

$$f_i \approx \sum_{j=1}^{N} \frac{m_j}{\rho_j} f_j W_{ij}, \tag{13}$$

$$\nabla f_i \approx \sum_{j=1}^{N} \frac{m_j}{\rho_j}(f_j \pm f_i)\nabla W_{ij}, \tag{14}$$

where m_j/ρ_j, $\langle f \rangle_i$ and $\langle \nabla f \rangle_i$ denote the number density (weight) of particle j, the kernel approximations of the field $f(\boldsymbol{x})$ and its gradient at position $\boldsymbol{x}_i$, respectively.

2.3. Stress description of solids and fluids

Equations (1)-(3) allow a common description of fluid and solid dynamics within the same framework [45]. This facilitates the treatment of multiple materials in complex physical problems, such as biological systems and multiphase flows. Different materials can then be modeled using different constitutive relations for the Cauchy stress tensor $\boldsymbol{\sigma}$. For validation purposes, we use two types of materials: linear elastic solids and Newtonian fluids. Thus,

$$\boldsymbol{\sigma} = \begin{cases} -P\boldsymbol{I} + \boldsymbol{S}, & \text{solids.} \\ -P\boldsymbol{I} + 2\eta\boldsymbol{\epsilon}, & \text{for fluids.} \end{cases} \tag{15}$$

where P, η are the pressure and viscosity, and $\boldsymbol{S}$, $\boldsymbol{\epsilon}$, $\boldsymbol{I}$ denote the deviatoric stress, strain and second-order identity tensors, respectively. Assuming Hooke's law, the Jaumann rate of the deviatoric stress tensor $\boldsymbol{S}$ is given by [44]

$$\frac{d\boldsymbol{S}}{dt} = 2G\left[\boldsymbol{\epsilon} - \frac{1}{3}\mathrm{Tr}(\boldsymbol{\epsilon})\boldsymbol{I}\right] + \boldsymbol{S}\cdot\boldsymbol{\omega}^T + \boldsymbol{\omega}\cdot\boldsymbol{S}, \tag{16}$$

where G is the shear modulus and $\boldsymbol{\omega}$ is the rotation tensor. The kernel approximations are used to discretize the spatial derivatives and primitive variables in the governing equations, Eqs. (1)-(3). The resulting equations are

$$\begin{aligned} \frac{d\rho_i}{dt} &= \rho_i \sum_j \frac{m_j}{\rho_j} \nabla W_{ij}\cdot \boldsymbol{v}_{ij} \\ &- \sum_j \frac{m_j}{\rho_j} \nabla W_{ij}\cdot[\rho_i(\boldsymbol{v}_i - \tilde{v}_i) + \rho_j(\boldsymbol{v}_j - \tilde{\boldsymbol{v}}_j)], \end{aligned} \tag{17}$$

$$\begin{aligned} \frac{d\boldsymbol{v_i}}{dt} &= -\sum_j m_j \nabla W_{ij}\cdot \\ &\cdot\left[\left(\frac{\boldsymbol{\sigma}_i}{\rho_i^2} + \frac{\boldsymbol{\sigma}_j}{\rho_j^2}\right) - \left(\frac{\mathbf{A}_i}{\rho_i^2} + \frac{\mathbf{A}_j}{\rho_j^2}\right)\right] \\ &+ \sum_j m_j \frac{\mu_{ij}}{\rho_i\rho_j(x_{ij}^2 + \epsilon h^2)} \nabla W_{ij}\cdot \boldsymbol{v}_{ij}, \end{aligned} \tag{18}$$

$$\begin{aligned} \frac{dC_i}{dt} &= \sum_j m_j \frac{\alpha_{ij}(C_j - C_i)}{\rho_i\rho_j(x_{ij}^2 + \epsilon h^2)} \nabla W_{ij}\cdot x_{ij} \\ &- \sum_j \frac{m_j}{\rho_j} \nabla W_{ij}\cdot[C_i(\boldsymbol{v}_i - \tilde{\boldsymbol{v}}_i) + C_j(\boldsymbol{v}_j - \tilde{\boldsymbol{v}}_j)], \end{aligned} \tag{19}$$

$$\begin{aligned} \frac{d\boldsymbol{S}_i}{dt} &= 2G\left[\boldsymbol{\epsilon}_i - \frac{1}{3}Tr(\boldsymbol{\epsilon}_i)\boldsymbol{I}\right] + \boldsymbol{S}_i\cdot\boldsymbol{\omega}_i^T \\ &+ \boldsymbol{\omega}_i\cdot\boldsymbol{S}_i, \end{aligned} \tag{20}$$

where the strain and rotation tensors for each particle i in Eq. (20) are given by

$$\boldsymbol{\epsilon}_i = \sum_j \frac{m_j}{2\rho_j}[\boldsymbol{v}_{ij} \otimes \boldsymbol{\nabla} W_{ij} + (\boldsymbol{v}_{ij} \otimes \boldsymbol{\nabla} W_{ij})^T], \tag{21}$$

$$\boldsymbol{\omega}_i = \sum_j \frac{m_j}{2\rho_j}[\boldsymbol{v}_{ij} \otimes \boldsymbol{\nabla} W_{ij} - (\boldsymbol{v}_{ij} \otimes \boldsymbol{\nabla} W_{ij})^T], \tag{22}$$

and the summations are performed over all neighboring particles of particle i that are within the compact support of W, and $\boldsymbol{v}_{ij} = \boldsymbol{v}_i - \boldsymbol{v}_j$. The term $\mathbf{A} = \rho \boldsymbol{v}(\boldsymbol{v} - \tilde{\boldsymbol{v}})$ denote the relative velocity tensor. The shear viscosity and mass diffusion coefficients are averaged as $\mu_{ij} = 2\mu_i\mu_j/(\mu_i + \mu_j)$ and $\alpha_{ij} = 2\alpha_i\alpha_j/(\alpha_i + \alpha_j)$. A small constant $\epsilon = 0.01$ is added to the denominators of Eqs. (18)-(19) to prevent singularities.

The second summation in Eq. (18), introduced by Morris et al. [47], improves the stability of the numerical method by acting as a diffusive term, while modeling the viscous force $\boldsymbol{F}_{\mathrm{V}}$, in a similar manner as the Von Neumann & Richtmyer's artificial viscosity term used in most standard SPH formulations [2, 48, 49], and has been used even for elastic solids [44]. In the present work, we have adopted the artificial viscosity formulation, but it is important to emphasize that the artificial viscosity term Eq.(18) is still an active area of research, and to a certain extent and despite being widely used in the classic SPH literature, its application makes the method case-dependent. A promising alternative to the artificial term consists in reformulating the SPH convolution integrals by introducing only the sufficient amount of dissipation by means of using a non-linear Riemann problem; this technique, named Godunov SPH (GSPH), is known for achieving very low advection and angular momentum conservation errors and no excessive diffusion, without the need for tuning artificial viscosity terms [50, 51, 52].

The model described by Eqs. (17)-(19) is closed by a relationship between the density and pressure field. For fluids, two different approaches are widely used in the literature, namely: 1) treat the flow as incompressible, either by solving a pressure-Poisson equation to obtain a divergence-free velocity field [53, 41], or by requiring as a kinematic constraint that the volume of the fluid particles is constant [54]; or 2) treat it as weakly compressible, and impose an equation of state [49, 55, 23, 22, 12, 13, 45]. We follow the weakly compressible formulation, with an equation of state of the form

$$P = P_0\left[\left(\frac{\rho}{\rho_0}\right)^\gamma - 1\right], \tag{23}$$

where P_0, ρ_0 denote reference pressure and density, respectively, and γ is the polytropic constant. It is a common practice [23, 13] to select $P_0 = K = \rho_0 c_0^2 / \gamma$, where c_0 is the artificial speed of sound and K is the compressibility modulus of the material. In order to limit density variations and prevent excessive spurious pressure waves [12], we choose $\gamma = 1$. Here, c_0 is chosen based on the desired Mach number, Ma, and the characteristic velocity of the problem U_c. For problems involving liquids, a typical choice is to use $Ma = 0.1$ to reduce compressibility effects, and thus $c_0 = 10\ U_c$. For solids, previous works [44, 56, 45]

have used the same formulation ($P_0 = \rho_0 c_0^2 / \gamma$), in which the sound speed of the solid is computed using the shear modulus G and Poisson ratio of the material, ν_p, as $c_0 = \sqrt{2G(1-\nu_p)/\rho_0}$.

In addition, for solid particles, we suggest the addition of an artificial stress term to Eq. (18), as described by Monaghan [44], as we found that the transport-velocity formulation was not capable of removing the tensile instability in solids completely without introducing excessive particle distortion.

2.4. Defining the transport velocity

The transport-velocity formulation introduces the velocity of the reference frame, $\tilde{\boldsymbol{v}}$, into Eqs. (6)-(8). This arbitrary velocity determines the nature of the reference frame, adjusting the conservation laws to an Eulerian, Lagrangian or any arbitrary mode in between these descriptions, therefore providing a arbitrary Lagrangian Eulerian (ALE) formalism to SPH [43].

We adopt the transport velocity correction term [22] as our arbitrary velocity, which has the form of a background pressure gradient

$$\tilde{\boldsymbol{v}}(t+\Delta t) = \boldsymbol{v}(t) + \Delta t\left(\frac{\tilde{d}\boldsymbol{v}}{dt} - \frac{1}{\rho}\nabla P_b\right), \tag{24}$$

where the background pressure gradient is discretized as

$$\boldsymbol{f}_{\mathrm{PB}} = \left(\frac{1}{\rho}\nabla P_b\right)_i \approx P_b \sum_j \frac{m_j}{\rho_i^2}\nabla W_{ij} \tag{25}$$

and P_b is chosen as the reference pressure, P_0. This choice is justified by the additional benefit that this term acts as a self-relaxation mechanism [46] in the linear momentum equation by balancing the actual hydrodynamic pressure gradient $\nabla P/\rho$ term, therefore reducing the tension instability in the flow and greatly improving the overall accuracy of the method.

2.5. Switch correction for pressure and filter

For fluid flows subject to large Reynolds numbers or shear effects, it has been reported that the usage of the continuity equation, Eq. (17) may result in errors and spurious pressure waves that deteriorate the accuracy of the numerical solution [57, 45]. In order to overcome this issue, Adami et al. [12] proposed the computation of the density via interpolation, which conserves mass exactly. Although these two formulations are mathematically equivalent [49], it has been shown that the usage of the continuity equation within an ALE framework results in smoother density fields [43]. However, experiments reported by Sun et al. [58] have shown that the pressure can still attain negative values, causing instabilities and numerical cavitation.

We propose the solution of the continuity equation, along with the usage of a pressure switch to address the numerical cavitation problem, which filters negative pressures. Both the filter

and the switch are used only for fluid particles, as negative pressures are required for compressive stress in solids. A similar procedure was proposed by Sun et al. [58]. This simple correction is based on the identity

$$\sum_j m_j \nabla W_{ij} \cdot \left(\frac{P_i}{\rho_i^2} + \frac{P_j}{\rho_j^2} \right) \mathbf{I} = \sum_j m_j \nabla W_{ij} \cdot \left(\frac{P_j}{\rho_j^2} - \frac{P_i}{\rho_i^2} \right) \mathbf{I} + 2 \frac{P_i}{\rho_i^2} \sum_j m_j \nabla W_{ij} \cdot \mathbf{I} \tag{26}$$

and proceeds by dropping the second sum in Eq. (26) if the pressure is negative, i.e.,

$$\left(\frac{1}{\rho} \nabla P \right)_i = \begin{cases} \sum_j m_j \nabla W_{ij} \cdot P_{ij}^{+} \mathbf{I}, \text{ if } P_{ij}^{+} \geq 0 \\ \sum_j m_j \nabla W_{ij} \cdot P_{ij}^{-} \mathbf{I}, \text{ else,} \end{cases} \tag{27}$$

where the pairwise pressures P_{ij}^{+} and P_{ij}^{-} are computed as

$$P_{ij}^{+} = \left(\frac{P_j}{\rho_j^2} + \frac{P_i}{\rho_i^2} \right), \tag{28}$$

$$P_{ij}^{-} = \left(\frac{P_j}{\rho_j^2} - \frac{P_i}{\rho_i^2} \right). \tag{29}$$

Finally, in order to damp high-frequency pressure waves and improve energy conservation, we use a Shepard filter in the density field every N_f timesteps [59]

$$\rho_i = \frac{\sum_j m_j W_{ij}}{\sum_j \frac{m_j}{\rho_j} W_{ij}}, \tag{30}$$

where the optimal frequency for filtering, $N_f = 20$, as reported by Colagrossi and Landrini [57], was used.

2.6. Temporal integration

Following the practice of several authors [44, 60, 12], the integration of Eqs. (17)-(20) was performed using a modified velocity-Verlet scheme. For the density and concentration fields, we have adopted an explicit midpoint method. Specifically, considering $\boldsymbol{v}_i$, $\boldsymbol{x}_i$, ρ_i, C_i, $\boldsymbol{S}_i$ the unknowns of the system, and f_ρ, $\boldsymbol{f}_v$, f_C, $f_{\boldsymbol{S}}$ the right-hand sides of Eqs. (17)-(20), respectively, the proposed numerical integration is given by

Step 1

a. Initial half-steps

$$\boldsymbol{\rho}^{n+1/2} = \boldsymbol{\rho}^{n} + \frac{\Delta t}{2} f_{\rho}^{n-1/2}, \tag{31}$$

$$\boldsymbol{v}^{n+1/2} = \boldsymbol{v}^{n} + \frac{\Delta t}{2} \boldsymbol{f}_{v}^{n-1/2}, \tag{32}$$

$$\tilde{\boldsymbol{v}}^{n+1/2} = \boldsymbol{v}^{n+1/2} + \frac{\Delta t}{2} \boldsymbol{f}_{\mathrm{PB}}^{n-1/2}, \tag{33}$$

$$C^{n+1/2} = C^{n} + \frac{\Delta t}{2} f_{C}^{n}, \tag{34}$$

$$\boldsymbol{S}^{n+1/2} = \boldsymbol{S}^{n} + \frac{\Delta t}{2} f_{\boldsymbol{S}}^{n}. \tag{35}$$

a. Position update

$$\boldsymbol{x}^{n+1} = \boldsymbol{x}^{n} + \Delta t\, \tilde{\boldsymbol{v}}^{n+1/2}. \tag{36}$$

Step 2

a. Final half-steps

$$\boldsymbol{\rho}^{n+1} = \boldsymbol{\rho}^{n} + \Delta t\, f_{\rho}^{n+1/2}, \tag{37}$$

$$\boldsymbol{v}^{n+1} = \boldsymbol{v}^{n+1/2} + \frac{\Delta t}{2} \boldsymbol{f}_{v}^{n+1/2} \tag{38}$$

$$C^{n+1} = C^{n} + \Delta t\, f_{C}^{n+1/2}, \tag{39}$$

$$\boldsymbol{S}^{n+1} = \boldsymbol{S}^{n} + \Delta t\, f_{\boldsymbol{S}}^{n+1/2}. \tag{40}$$

Although the method has two steps, notice that it requires the evaluation of the particle forces only once per time step. A necessary condition for stability, given by the Courant-Friedrichs-Lewy condition based on the artificial speed of sound c_0, was used to estimate a suitable time step Δt for each simulation [13]

$$\Delta t \leq C \min\left(\frac{h}{c_0 + |U_c|}, \frac{h^2 \rho}{\mu}, \sqrt{\frac{h}{g}}\right), \tag{41}$$

where g is the gravity acceleration, and a Courant number $C = 0.25$ was adopted.

3. Wall treatment: boundary volume fraction method

We start by considering a particle of fluid i, located at a weighted averaged distance d from the wall. As depicted in Fig. 1, the region of influence around particle i, denoted by Ω, has radius h. The shaded region represents the solid wall. We denote the intersection of wall and region Ω by S.

We assume that the curvature of the wall, κ_{wall}, is far smaller than the curvature of Ω, κ_{Ω}. Following Li et al. [37], we assign to particle i an extra variable, denoted by ϕ. We define ϕ as the ratio between the volumes of regions S and Ω, i.e., the boundary volume fraction (BVF), given by

$$\phi := \frac{V^S}{V^\Omega}. \tag{42}$$

Notice that, for $d = 0$, the particle i is located exactly at the wall, and thus $\phi = 0.5$. This allows us to use the variable ϕ to act as an indicator function of how close a particle is from the solid wall. It is important to highlight that the boundary volume fraction interface cutoff of 0.5 makes sense only within a predictor-corrector temporal integration scheme, as the theoretical value of $\phi = 0.5$ at the interface is never met due to numerical precision. Thus, the particle will have its trajectory corrected (in the corrector step) only when it reaches the wall (in the predictor step). Nevertheless, pairwise and viscous effects of the wall particles remain in effect within the cutoff of the kernel function adopted, as in other SPH methods.

Assuming that both the wall and the support domain Ω have sufficient particles, we can approximate the volumes of regions S and Ω in Eq. (42) using the SPH formalism

$$V_i^S = \sum_{j \in S} \frac{m_j}{\rho_j} V_j W_{ij} = \sum_{j \in S} \left(\frac{m_j}{\rho_j}\right)^2 W_{ij}, \tag{43}$$

$$V_i^\Omega = \sum_{j \in \Omega} \frac{m_j}{\rho_j} V_j W_{ij} = \sum_{j \in \Omega} \left(\frac{m_j}{\rho_j}\right)^2 W_{ij}, \tag{44}$$

where Ω is the total set of particles, and S the subset of solid particles. Thus, the BVF of particle i, ϕ_i, written in terms of SPH formalism is given by

$$\phi_i = \frac{\sum_{j \in S} \left(\frac{m_j}{\rho_j}\right)^2 W_{ij}}{\sum_{j \in \Omega} \left(\frac{m_j}{\rho_j}\right)^2 W_{ij}}. \tag{45}$$

Compared to the standard SPH algorithm, the only major modification regarding the wall treatment in the SPH-BVF method is that the numerical integration of Eqs. (1)-(3) now includes an additional constraint: the following correction is performed in the velocity field of particle i if $\phi_i \geq 0.5$, i.e., if particle i penetrates the wall, we correct the velocity of particle

i by reassigning its velocity to the value calculated using the bounce-back equation proposed by Li et al. [37]

$$\boldsymbol{v}_i^{\text{corrected}} = 2\boldsymbol{v}_i^{\text{wall}} + \Delta t \boldsymbol{a}_i^{\text{wall}} - \boldsymbol{v}_i + 2\max(0, \boldsymbol{v}_i \cdot \boldsymbol{e}_i^n)\boldsymbol{e}_i^n, \tag{46}$$

where $\boldsymbol{e}^n = \boldsymbol{n}^\omega / n^\omega$ denotes the unit normal vector pointing outward from the wall boundary, Δt is the time step and $\boldsymbol{v}^{\text{wall}}$, $\boldsymbol{a}^{\text{wall}}$ are the local velocity and acceleration of the boundary, respectively. This equation results from the collision of two particles of arbitrary masses as described in Lifshitz et al. [61] in the limit case where one particle possesses much greater mass ($m_1 \gg m_2$) so that the inertial effects on the larger particle are negligible compared to the smaller particle bouncing-back. Because the collision is considered elastic, the conservation of energy is preserved. The normal vector for particle i, $\boldsymbol{n}_i^w$, is given by the gradient of $\boldsymbol{\phi}_i$:

$$\boldsymbol{n}_i^w = \frac{\sum_{j \in S} \left(\frac{m_j}{\rho_j}\right)^2 \nabla W_{ij}}{\sum_{j \in \Omega} \left(\frac{m_j}{\rho_j}\right)^2 W_{ij}}. \tag{47}$$

Li et al. [37] suggest the approximation of the local wall velocity and acceleration of moving boundaries, $\boldsymbol{v}_i^{\text{wall}}$, $\boldsymbol{a}_i^{\text{wall}}$ as the velocity of the nearest wall particle. To increase the accuracy of this approximation, we propose the usage of a kernel-interpolated velocity and acceleration of solid particles. Thus, for a fluid particle i, its neighbor solid moves with

$$\boldsymbol{v}_i^{\text{wall}} = \frac{\sum_{j \in S} \boldsymbol{v}_j \left(\frac{m_j}{\rho_j}\right)^2 W_{ij}}{\sum_{j \in S} \left(\frac{m_j}{\rho_j}\right)^2 W_{ij}}, \tag{48}$$

$$\boldsymbol{a}_i^{\text{wall}} = \frac{\sum_{j \in S} \boldsymbol{a}_j \left(\frac{m_j}{\rho_j}\right)^2 W_{ij}}{\sum_{j \in S} \left(\frac{m_j}{\rho_j}\right)^2 W_{ij}}, \tag{49}$$

where the summations in Eqs. (48)-(49) are over the solid wall particles in the support of particle i (S).

Algorithm 1 SPH-BVF method

Input: Given initial positions, velocities and concentrations of species for all particles i at time t: $\boldsymbol{x}_i, \boldsymbol{v}_i, C_i$, and integration timestep Δt.

Output: Positions, velocities and concentrations of species for all particles i at time $t + \Delta t$.

Find forces, for all i:
for all i **do**
  Compute SPH approximations, Eqs. (17)-(19).
  Compute ϕ_i, Eq. (45).
end for
Perform temporal integration, for all i:
for all i **do**
  After the modified velocity-Verlet final integration step (**Step 2**), perform BVF correction:
  if $\phi_i \geq 0.5$ **then**
    $\boldsymbol{v}_i \leftarrow 2\boldsymbol{v}_i^{\text{wall}} + \Delta t \boldsymbol{a}_i^{\text{wall}} - \boldsymbol{v}_i + 2\max(0, \boldsymbol{v}_i \cdot \boldsymbol{e}_i^n)\boldsymbol{e}_i^n$
  end if
end for

Notice that the accuracy of the computation of the normal vector and the BVF is strictly dependent on having enough particles to accurately represent the walls. Thus, thin walls, regions of large curvature and large particle spacing among wall particles are some of the limitations of the BVF method. In practice, we have found that three layers of particles are typically enough to obtain accurate results, while slightly increasing the computational load of the method. However, the overall computational cost for the present method must have the same order of magnitude as standard SPH, since the only algorithmic addition in SPH-BVF is computing the normals and the additional BVF field $\boldsymbol{\phi}_i$ in Eq. (47), which can be performed in parallel with the evaluation of the pairwise forces, with the advantage that fluid particle penetration is explicitly avoided. A review of the algorithm is provided in Algorithm 1.

3.1. Implementation

The SPH-BVF method summarized in Algorithm 1 was implemented in a stable version of the open-source Large-scale Atomic/Molecular Massively Parallel Simulator (LAMMPS) [62] (v.22 Aug 2018). Originally developed as a molecular dynamics code, LAMMPS can also be used as a library to develop new particle-based methods. The code features an efficient particle neighbor search algorithm based on Verlet lists. Our source code, along with instructions to reproduce the validation cases and the motivation problem are available at the Github page: https://github.com/briandrawert/SPH-BVF/, under a GPL v2.0 license.

4. Validation

In this section we validate the SPH-BVF method using several canonical examples.

First, a Poiseuille flow simulation is used to validate and verify the convergence of the fluid flow solver and the BVF boundary conditions. In addition, the new method is tested for different kernels. In our second example we validate our method with the Taylor-Green vortex flow problem and compare the results with the standard SPH method, showing that the SPH-BVF method resolves the velocity decay accurately, without excessive diffusion. Next, a lid-driven cavity flow is used to validate the fluid flow solver and the BVF wall boundary conditions, which further validates our method over a wider range of Reynolds numbers and demonstrates that fluid particles do not penetrate through the walls. We validate the strong coupling of fluid flow and mass transport with a natural convection flow, emphasizing the elimination of tensile instabilities and particle alignments, and also demonstrating our method on curved walls. In our fifth example, we validate SPH-BVF for solid mechanics with an oscillating cantilever beam. This problem demonstrates the use of our method on a moving solid under tension, and further shows the elimination of tensile instability. Finally, we compare SPH-BVF with a finite element method using a fluid-structure interaction problem. This example also demonstrates our method in the context of sponge zones and flux boundary conditions.

4.1. Wall boundary condition validation: Poiseuille flow

We validate the proposed wall boundary condition method with a laminar, two dimensional Poiseuille flow in a closed channel as performed by Ferrand et al. [63]. The flow is driven by a constant volume force of magnitude 0.8 $[ms^{-2}]$, and periodic boundary conditions are imposed in the streamwise (x)-direction. The channel width is assumed to be $W = 1\ [m]$, where a fluid with viscosity $\nu = 10^{-1}\ [m^2 s^{-1}]$ flows with a resulting Reynolds number $Re = 10$. We have considered five different particle refinements, with $N_y = 20$, 40, 80, 160 and 320 particles in the cross-stream (y)-direction. In addition to the standard Lucy kernel given by Eq. (10), we have performed convergence studies using the cubic spline kernel [44] and the Wendland quintic kernel [64]. In all cases, the kernel cutoff is set to $h = 3\Delta p$, which for a support of diameter $2h$ results in approximately 28 neighbors, and Δp is the particle spacing.

For a fully-developed, steady-state flow, the analytical velocity profile of the flow in the streamwise direction, v_x^{a}, is given by

$$v_x^{\mathrm{a}}(y) = 4\, Re\, \nu \frac{y}{W^2}\left(1 - \frac{y}{W}\right), \tag{50}$$

Based on these levels of particle refinement, and using the analytical solution given by Eq. (50), we have performed a convergence study, taking as an error metric the L_2 norm of the global error [63, 65]

$$L_2\,\text{error} = \sqrt{\frac{1}{N_f} \sum_{i \in \text{fluid}} \left(v_x^{\mathrm{a}}(y_i) - v_{x,i}^{\mathrm{sph}}\right)^2}, \tag{51}$$

where N_f refers to the total number of fluid particles used in the L_2 error summation.

The errors obtained from the convergence study are provided in Table 1. The streamwise velocity profile of the flow is shown in Fig. 2-(a) for all the refinement levels. As reported in Ferrand et al. [63], we noticed that the error of the proposed BVF boundary condition has a non-constant slope, oscillating between first and second order convergence, as is observed under the Lennard-Jones and fictitious particles boundary conditions. This behavior is depicted in Fig. 2-(b). This result is expected because no kernel correction technique was enforced near the boundary, which also justifies the slower convergence behavior of the shear rate near the wall, as depicted in Fig. 2-(c). In terms of accuracy, the Lucy kernel performed better than both the cubic spline and Wendland kernels. We found the Wendland kernel produced more organized particles, but that did not translate into a higher convergence order. Thus, based on the superior accuracy and simplicity, we have opted to use the Lucy kernel hereafter.

4.2. Analytical solution validation: 2D Taylor-Green vortex

The Taylor-Green flow is a closed form solution of the incompressible Navier-Stokes equations, and is widely used to validate fluid flow solvers. It consists of the decaying of a vortex due to viscous effects of the fluid, and is given by the following analytical velocity fields [12]

$$v_x^{\mathrm{a}}(x^*, y^*, t^*) = -Ue^{bt^*}\cos(2\pi x^*)\sin(2\pi y^*), \tag{52}$$

$$v_y^{\mathrm{a}}(x^*, y^*, t^*) = Ue^{bt^*}\sin(2\pi x^*)\cos(2\pi y^*), \tag{53}$$

where b is the decay rate of the velocity field and U is the maximum initial velocity. We use Eqs. 52-53 to estimate the accuracy of the SPH-BVF method. In our simulations, we assume a Reynolds number $Re = UL/\nu = 100$, a maximum velocity $U = 1$, a decay rate $b = -8\pi^2/Re$ and a domain of length $L = 1$. The boundary conditions are periodic in both directions, with $x^*, y^* \in [0, 1] \times [0, 1]$. The initial conditions are obtained by setting the dimensionless time $t^* = tU/L = 0$ in Eqs. 52-53. The unit length domain is discretized using three levels of equally-spaced particle refinements: $N = 50^2$, 100^2 and 200^2. For each simulation, the relative error of the numerical solution is measured over time using the L_∞ norm, given by

$$L_\infty(t^*) = \left| \frac{\max_i(\|\boldsymbol{v}_i(t^*)\|) - Ue^{bt^*}}{Ue^{bt^*}} \right|. \tag{54}$$

Figure 3 shows snapshots of the particles at dimensionless times $t^* = 0.1, 0.5$ for the case of $N = 50^2$. The top figures (a,b) show the results for the standard SPH, and the bottom figures (c,d) correspond to results from the present method (SPH-BVF). In (a,b), it is possible to visualize the anisotropic particle alignment caused by tensile instability. This alignment causes excessive diffusion, leading to a fast decay of the velocity field. In contrast, the results obtained by the SPH-BVF method (c,d) dramatically reduce the particle alignments

and tensile instabilities, thus preserving the velocity decay. Remarkably, we found that the SPH-BVF method was able to prevent tensile instabilities even in the case of an initial regular lattice particle distribution. No significant differences were observed for other arrangements of particles (data not shown), including randomly shifted arrangements. Conversely, in the work of Adami et al. [12], it was found that the original transport-velocity formulation was sensitive to the initial particle distribution. We believe that our method does not suffer from this sensitivity, thus resulting in a more accurate velocity decay.

The velocity decay is shown in Fig. 4. We compare our results with the exact solution Ue^{bt^*} and plot the maximum velocity for all three particle refinements ($N = 50^2, 100^2, 200^2$). Following [12], we also compare our method with standard SPH, showing that the latter fails to predict the exact decay. In contrast, the SPH-BVF method accurately predicts the decay, even for the coarser refinement ($N = 50^2$). Compared to [12], the SPH-BVF method appears to not suffer from the shifted profile obtained by the original transport-velocity formulation.

In addition to the velocity decay, the temporal evolution of the L_∞ norm, Eq. (51), is shown in Fig. 5. The relative error of the maximum velocity, L_∞, is ≈ 2% for all tested cases. This result is comparable to the best results obtained by [12] (non-regular initial particle distribution, $N = 200^2$). Remarkably, the SPH-BVF method was able to achieve excellent results even at the lowest resolution ($N = 50^2$, equally spaced, regular lattice particle distribution).

4.3. Fluid mechanics validation: lid-driven cavity flow

The lid-driven cavity flow is a classical model problem, and is considered a challenging problem to be solved using SPH [22]. We validate the proposed method using the high-resolution finite difference numerical experiment carried out by Ghia et al. [66]. It consists of a square cavity of side L, filled with a Newtonian fluid of kinematic viscosity $\nu = \mu/\rho$. Gravity effects are considered negligible. In Fig. 6(a), the schematic of the lid-driven cavity flow is presented.

The flow, initially at rest, is induced by shear as the lid of the cavity starts moving at uniform velocity v_0. The governing equations are nondimensionalized, in order to validate our results with the reference. The dimensionless groups are given by

$$x_o = L, \tag{55}$$

$$t_o = x_o / v_o, \tag{56}$$

$$P_o = \rho_o v_o^2, \tag{57}$$

where ρ_o is a reference density, considered here as unity. Using these groups, Eqs. (1)-(3) are rewritten as

$$\frac{d\rho^*}{dt^*} = -\rho^* \nabla^* \cdot \boldsymbol{v}^*, \tag{58}$$

$$\frac{d\boldsymbol{v}^*}{dt^*} = -\nabla^* p^* + \frac{1}{Re} \nabla^{*2} \boldsymbol{v}^*, \tag{59}$$

where $Re = v_0 L/\nu$ denotes the Reynolds number with respect to the characteristic length L. The walls of the cavity are modeled using three layers of fixed solid particles, so that near-wall fluid particles are guaranteed to have enough support for accurate ϕ_i computations.

To test the convergence of the method, simulations were performed using three levels of particle refinement ($N = 50^2$, 100^2, 200^2 particles) for each Reynolds regime ($Re = 100$, 1000, 10000), resulting in a total of nine simulations. In all cases, we have used the Lucy kernel, with cutoff $h = 2.6\Delta p$. We assumed that steady-state was reached once the total kinetic energy of the system was constant over time within a 10^{-3} tolerance.

An overview of the flow dynamics on the lid-driven cavity is provided in Figs 9(b)-(c), showing the isocontours of the flow velocity magnitude for each Reynolds flow regime using $N = 200^2$ particles. Figure 7 shows the vertical and horizontal velocity profiles for all three levels of particle refinement. For $Re = 100$, the method provides results comparable to the reference, even for the smallest particle refinement, $N = 50^2$. For $Re = 1000$, the SPH-BVF results converge to the reference values. Notice that for $N = 200^2$ particles, the results are very close to those of the reference, even though Ghia et al. [66] used a higher resolution (257^2 mesh). For $Re = 10000$, it is possible to infer the convergence to the reference solution as the refinement level increases. Nevertheless, as observed by Adami et al. [12], a deviation from the reference data is observed, which can be justified by the requirement of a higher refinement level and by the lack of turbulence modeling. For $Re > 10000$, the flow does not converge to a steady-state [66].

Figure 8 shows the streamlines in the cavity for $Re = 1000$, revealing the two main structures of the flow: the left and right corner vortices. In his work, Ghia et al. [66] reported approximated heights of 0.15 and 0.35 for the left and right corner vortices, respectively (c.f. Fig. 8). Similarly, the expected values for the widths are approximately 0.20 (left) and 0.30 (right). The sizes of the vortices obtained by our simulations agree with the reference, showing that the SPH-BVF method was able to accurately predict these vortices, therefore validating the wall boundary formulation.

4.4. Convective transport validation: natural convection

We validate the coupling of advection-diffusion using a coupling force, based on the Oberbeck-Boussinesq approximation [67], in the context of the transport-velocity formulation. To the authors' best knowledge, this is the first time an ALE formulation of SPH has been used to simulate convection. A classical test case widely used in the literature is the natural convection over a cylinder immersed in a square cavity. A complete description of the problem is given in Fig. 9. The system consists of a square enclosure, filled with fluid

at rest. The wall boundaries of the cavity and in the interface between the cylinder and the fluid are modeled with non-moving SPH particles to enforce the no-slip boundary condition. Initially, the fluid is free of solute, i.e., $C(\mathbf{x}, 0) = 0$. At $t > 0$, the wall concentrations of solute in the circular cylinder and at the enclosure walls are set to C_C and C_E, respectively. Since $C_E > C_C$, mass transfer begins to occur, and the system is treated as a binary mixture. The solute diffuses in the fluid over time, leading to mass stratification.

The Oberbeck-Boussinesq approximation is used to describe the mass transport phenomena, such that a driven body force is proportional to the variation of concentration C, gravity acceleration g and coefficient of mass expansion β. In this case,the body force in Eq. 2 takes the form

$$\boldsymbol{F}_{\mathrm{B}} = g\beta\Delta C\,\hat{\boldsymbol{e}}_y, \tag{60}$$

where $\Delta C = C - C_{\mathrm{ref}}$, C_{ref} is a reference concentration and $\hat{e}_y$ is the y-direction component of the standard Cartesian basis, $(\hat{e}_x, \hat{e}_y, \hat{e}_z)$.

The problem was addressed in previous works as natural convection of heat [68, 69, 70, 71], and has been tested in many different geometries [69, 72, 73, 74]. In order to validate results with the work of Moukalled and Acharya [68], the equations are rendered dimensionless, using the reference groups proposed by Gray and Giorgini [67]

$$x_o = L, \tag{61}$$

$$v_o = \sqrt{g\beta L\Delta C}, \tag{62}$$

$$t_o = x_o \,/\, v_o, \tag{63}$$

$$\Delta C_o = C_C - C_E, \tag{64}$$

$$P_o = \rho_o v_o^2, \tag{65}$$

where ρ_o is a reference density, considered here as unity. Using these groups, Eqs. (1)-(3) are rewritten as

$$\frac{d\rho^*}{dt^*} = -\rho^*\boldsymbol{\nabla}^* \cdot \boldsymbol{v}^*, \tag{66}$$

$$\frac{d\boldsymbol{v}^*}{dt^*} = -\boldsymbol{\nabla}^* P^* + \sqrt{\frac{Sc}{Ra}}\boldsymbol{\nabla}^{*2}\boldsymbol{v}^* + C^*\hat{\mathbf{e}}_y, \tag{67}$$

$$\frac{dC^*}{dt^*} = \frac{1}{\sqrt{RaSc}} \nabla^{*2} C^*, \tag{68}$$

where $Sc = \nu/\alpha$ and $Ra = g\beta\Delta CL^3/\nu\kappa$ denote the Schmidt and mass transfer Rayleigh numbers, respectively.

Simulations were performed for $Ra = 10^4$, 10^5 and 10^6. The Schmidt number was taken to be equal to 0.7, and the cylinder diameter as $D = 0.2L$. For all the cases, the same number of particles N and same initial conditions were provided. The initial setup consists of $N = 200^2$ equally-spaced particles distributed in a squared domain of length $L = 1$. In all cases, we have used the Lucy kernel, with cutoff $h = 2.6\Delta p$. Boundary conditions are imposed using three layers of boundary particles in the walls. The cylinder at the center of the cavity is considered a boundary. Dirichlet boundary conditions are imposed by directly setting the concentration of boundary particles. As in the cavity flow, we assumed that steady-state was reached once the total kinetic energy of the system was constant over time within a 10^{-3} tolerance.

Profiles of the dimensionless concentration, C^*, and y-velocity component, v_y^*, are shown in Figs. 10a-10b. Results were compared with the numerical simulation of Moukalled and Acharya [68]. Since Moukalled and Acharya [68] use a different normalization for the velocity, the dimensionless velocity $\boldsymbol{v}^*$ obtained from the solution of Eq. (67) must be re-scaled, by multiplying $\boldsymbol{v}^*$ by $\sqrt{Ra\,/\,Sc}$.

As depicted in Figs. 10a-10b, satisfactory results were obtained for all of the Ra regimes. The method was also capable of capturing the stratification of the concentration profiles between the wall and the cylinder surface at $Re = 10^5$ and the concentration inversion that occurs at $Ra = 10^6$, which causes the flow to slow down in the interval $0.65 \lesssim x^* \lesssim 0.85$.

A comparison between the mean velocity fields obtained using the present method and standard SPH for $Ra = 10^6$ is shown in Fig. 11. While the results obtained by the standard SPH method have serious particle voids, penetration in the walls and in the cylinder, clumping and alignments, the SPH-BVF method mitigated all of these problems, while improving stability. The time step required for a stable simulation with SPH-BVF ($\mathcal{O}(10^{-4})$) was two orders of magnitude larger than the one required in practice using standard SPH, as the soundspeed must be increased to help mitigate the tension instability.

4.5. Solid mechanics validation: oscillating cantilever beam

We validate the solid mechanics part of the method with the test case of an oscillating cantilever beam. The problem consists of a thin plate of length L and thickness H, fixed on one edge and free on the other edges, as shown in Fig. 12.

The plate, initially at rest, is set to oscillate at one of its fundamental modes, namely at $kL = 1.875$ [56]. For different modes, other wavenumbers k can be found using the eigensolutions of the Euler-Bernoulli beam equations, given by

$$\cos(kL)\cosh(kL) = -1\,. \tag{69}$$

For the mode $kL = 1.875$, the resulting initial velocity profile is perpendicular to the plate and is given by

$$v_y^0(x) = V_0 c_0 \frac{F(x)}{F(L)}, \tag{70}$$

where V_0 is the magnitude of the velocity, c_0 is the soundspeed of the material and F is a force that varies along the length of the plate (x-direction)

$$\begin{aligned} F(x) = {} & [\cos(kL) + \cosh(kL)][\cosh(kx) - \cos(kx)] \\ & + [\sin(kL) - \sinh(kL)][\sinh(kx) - \sin(kx)]\,. \end{aligned} \tag{71}$$

In order to allow a direct comparison with the previous results of Zhang et al. [45], we set the plate properties using a Poisson ratio $\nu = 0.3975$, density $\rho = 1 \times 10^3 [kg/m^3]$ and Young's modulus $E = 2.0 \times 10^6 [Pa]$. We have performed simulations for initial velocity amplitudes $V_0 = 1 \times 10^{-3}$, 1×10^{-2} and $3 \times 10^{-2} [m/s]$. The artificial stress coefficient [44] is set to 0.2. In all cases, we have used the Lucy kernel, with cutoff $h = 3.0\Delta p$. The fixed support of the plate is constructed with stationary solid particles. For geometrical consistency, thickness of the upper and lower parts of the support were set to $T = H/2$.

Figure 13-(a) shows a convergence study based on the y-position of the centerline point of the beam at the tip ($x = L$). Results are in good agreement with previous studies [56, 45], and no numerical fracture is observed in the regions of maximum tension, as shown in Figure 13-(b), demonstrating that the tension instability was controlled and allowed large deformations of the beam.

A quantitative comparison with the analytical solution of a flat plate [61] for various velocity amplitudes V_0 and a relative error convergence analysis are shown in Table 2. The present method achieved relative errors of less than 1% for $N_y = 30$ and all values of V_0 compared to the 13% errors reported by Zhang et al. [45].

4.6. Comparison with FEM: fluid-structure interaction

As a final comparison, we demonstrate the ability of the SPH-BVF method to perform simulations of fluid-structure interaction (FSI) problems. The problem, depicted in Fig. 14, consists of a horizontal microchannel flow with a narrow vertical rod as an obstacle. A uniform fluid flow is introduced in the channel entry. In the region near the obstacle, the flow is induced into a narrow path in the upper part of the channel, and as a consequence it imposes a force on the structure's walls. The rod, made of a deformable material, bends under the applied load, reaching a steady state.

The wall boundary condition treatment in the SPH-BVF simulations follows the previous validation examples, with wall boundary conditions imposed using three layers of boundary particles in the walls. To model the inlet and outlet boundaries, we adopt the following

strategy: as the fluid leaves the channel, it is re-inserted back at the inlet after it passes through a sponge zone, which acts as a non-reflective boundary condition [75] to the flow and re-align the velocity profile. This strategy makes the computation less intensive as there is no need to destruct particles as they leave the domain, or to create new ones at the inlet, as doing so would require re-creating the particle neighboring list every time step. For details on the implementation of the sponge zone, we refer the reader to Drawert et al. [76].

Since the problem has no analytic solution, we compare our numerical simulation with high-resolution FEM using the FSI package in Comsol Multiphysics (v.5.3). The physical parameters for both FEM and SPH-BVF simulations are given in Table 3.

The SPH-BVF simulation was performed using 30, 000 fluid particles (representing the water) and 500 solid particles (representing the rod). The FEM solution was obtained using second-order shape functions in a mesh of approximately 12,000 elements. We assumed that steady-state was reached once the kinetic energy of the fluid flow was constant over time within a 10^{-3} tolerance.

Contour plots of the streamwise (v_x) and cross-stream (v_y) velocity components at steady-state are shown in Figs. 15-(a) and (b). Is possible to see the bending of the beam to the right, as a consequence of the flow, as well as boundary layer in the near-wall regions of the channel. To validate the velocity profiles, a probe was placed along the y-centerline of the channel.

Figures 15-(c) and (d) shows the velocity profiles of the channel at the probe, and a comparison with the FEM result. It is important to highlight that the comparison of velocity profiles in FEM and SPH-BVF agree in magnitude, demonstrating that the formulation for the non-reflexive boundary condition is satisfactory, as well as in phase, which demonstrates that the point of maximum deflection obtained in both FEM and SPH-BVF solutions are very close. However, notice that the stream-wise velocity v_x drops at the end of the channel, due to the presence of the sponge zone. Further investigations in non-reflective boundary conditions in SPH are required to improve these results.

5. Application: polarized yeast cell under-going mating projection growth

To further demonstrate the capability of the proposed method, we apply SPH-BVF to a biomechanics problem that poses a challenge for classic SPH as well as mesh-based methods because it involves deforming boundaries under pressure fluid-structure interaction, particle non-penetration and a conjugate transport mechanism (diffusion of chemical species that alters the mechanical properties of the material). The first attempt to simulate the mechanics of biological cells was performed by [77, 78], using an SPH-DEM hybrid method to study the mechanical response of plant cells under compression. The model, however, is purely mechanical, and therefore the reaction-diffusion dynamics of species in the cell wall are not considered.

The motivating problem is the growth of the mating projection in a yeast cell (*S. cerevisiae*) responding to mating pheromone in the extracellular fluid [79]. The key structure is the cell wall, which defines the shape of the cell while providing the mechanical integrity necessary

to withstand the large internal turgor pressure [80]. As depicted in Fig. 16, under the isotropic turgor pressure, polarized growth occurs via localized softening of the cell wall by the enzymatic digestion of the polymer crosslinks, inducing expansion at the tip. A mechanical feedback pathway delivers new wall material to this growing region by vesicular transport leading to expansion of the mating projection at the area targeted by the wall-modifying enzyme [81]. This problem demonstrates our method on curved and dynamically changing boundaries representing the cell wall. Importantly, the interior fluid, the cytoplasm, does not penetrate the cell wall even while under sufficient pressure to cause the wall to change shape.

5.1. Simplified model of yeast mating projection

Yeast mating projection growth is a classic example of cell polarization, and has been investigated experimentally [82, 83, 84] and through mathematical modeling [85, 86, 87]. Existing models have focused primarily on the reaction-diffusion dynamics of the signal transduction system. However, more recent work has highlighted the complex interplay between the biochemical dynamics within the mating projection and the mechanical forces acting on the cell wall to determine the shape of the cell [81]. It is important to note that the properties of biological materials involved are not well-characterized. For example, recent studies [88, 89] showed that cytoplasm can assume different properties, changing from a viscous fluid to an elastic solid, and can be considered compressible or incompressible, depending on the state of tension, biological process involved and external perturbations. Given that the SPH-BVF method is currently limited to linear elastic solids and Newtonian fluids, we assume that the cytoplasm is a compressible fluid, and that the cell wall is a linear elastic material characterized by a shear modulus. Finally, the extracellular fluid around the cell possesses the rheological properties of water.

For simplicity, we employ the following approximation of the coupling between the mechanical and biochemical systems. In the model, cell wall modifying enzymes, whose concentration is denoted by the variable c, decrease the shear modulus of the cell wall according to the following linear equation: $G(c) = G_0(1 - cR)$, in which R is a parameter representing wall degrading enzymatic activity, and G_0 is the reference shear modulus of the non-polarized wall region. The modifying enzymes are able to diffuse in the wall with a diffusion constant given by κ_c.

Even under these simplifying assumptions, the model is still complex enough that advanced computer-aided engineering (CAE) tools have difficulty simulating the coupled problem. For example, COMSOL (v.5.3a) is not capable of simulating dynamic mechanical properties coupled with diffusive transport in a moving mesh, and hence no direct comparison could be made.

5.2. Results

To demonstrate that SPH-BVF can simulate yeast mating projection growth, we chose to vary the diffusion coefficient κ_c of the wall-modifying enzymes using two different values. The other parameters were kept constant with the enzyme initially distributed in a region of width $H = \delta/2$, where δ is the cell wall thickness. The initial enzyme concentration was set

to be $c = 1$ [mol/m^3] in this region, and to $c = 0$ [mol/m^3] in the rest of the cell wall. The enzyme affects the shear modulus of the cell wall according to the linear relationship described above as it diffuses from its initial site. A list of the physical parameters used in the simplified model is provided in Table 4, and a reference table with each case is detailed in Table 5.

Figure 17 shows snapshots of the two simulations (cases I and II) at the two diffusion values. Interestingly, the larger diffusion constant produced a longer, laterally concave projection, whereas the smaller diffusion constant preserved its laterally convex shape. One can compare the simulations to time-lapse microscopy images obtained by exposing yeast cells to the mating pheromone α-factor. The cells contain the secretion marker Fus1-GFP which indicates the presumptive location where the wall-modifying enzymes are deposited on the cell wall [90]. Qualitatively speaking, the simulations were able to capture the general shape changes during projection growth, even though some level of particle alignment is observed near the boundary of the cells. One promising way of alleviating this effect is to use an optimal particle arrangement [91], which directly ensures the isotropy of the particle distribution, even without parameter tuning. Regardless, this example demonstrates the potential of the SPH-BVF method to simulate complex biological processes including both biochemical and physical spatial dynamics, involving fluid-structure interactions and materials with time-varying mechanical properties without inducing particle penetration or excessive tension instability.

6. Conclusion

We introduce a unified framework to simulate solid and fluid mechanics with convective reaction-diffusion transport in SPH. The method, named SPH-BVF, provides a new local wall boundary condition treatment for SPH, which allows particles to become autonomous to detect solid neighbors. The boundary volume fraction (BVF) approach introduces only a small computational overhead, while explicitly preventing fluid penetration through solid boundaries. In addition, SPH-BVF provides good accuracy and improved stability, and due to its ALE formulation, prevents tension instabilities and anisotropic particle alignments.

We have implemented our method within the LAMMPS [62] package. LAMMPS is a software package for simulation of classical molecular dynamics problems and is extensible to other particle-based methods. We have implemented the SPH-BVF method as a user module in LAMMPS. The complete code, along with all of the validations, post-processing routines and the application problem are also available in our source, under the GPL v2.0 license, which is the same license as the LAMMPS software package. For ease of replication of our results, we have packaged the solver and our examples as a Docker container https://hub.docker.com/r/briandrawert/sph_bvf/. Directions on how to use this container and the full source code are found on Github: https://github.com/briandrawert/SPH-BVF/.

While addressing some problems encountered by standard SPH, our method also possesses certain limitations. Simulations require approximately three layers of particles to have sufficient support within the kernel integration area to accurately estimate the boundary volume fraction. As a result, systems with very thin walls may require finer discretization

and more particles, which can lead to higher computational costs. One promising approach to overcome this issue in the future is the usage of an immersed boundary method to represent slender bodies [92, 93]. We also note that the proposed BVF boundary condition has a non-constant order of convergence (between first and second order), which is similar to the Lennard-Jones boundary condition using ghost particles.

One promising domain for SPH-BVF is in simulating biophysical systems. Specifically, we envision its application in the modeling of cell dynamics, as well as in other applications, such as intercellular junction formation, cell morphogenesis and blood flow simulations in tissues coupled to inter- and intra-cellular processes, in which conjugate transport, materials with dynamic mechanical properties and boundary deformation are relevant.

Acknowledgments

The authors acknowledge research funding from National Institutes of Health (NIH) NIGMS Award No. R01-GM113241 and NIBIB Award No. 2-R01-EB014877-04A1. We acknowledge support from the UCSB Center for Scientific Computing from the CNSI, MRL: an NSF MRSEC (DMR-1121053) and NSF CNS-0960316 for computational resources. The content of the information does not necessarily reflect the position or the policy of the funding agencies, and no official endorsement should be inferred.

References

[1]. Liu MB, Liu GR, Smoothed particle hydrodynamics (SPH): an overview and recent developments, Archives of Computational Methods in Engineering 17 (2010) 25–76.

[2]. Gingold R, Monaghan J, Smoothed particle hydrodynamics - Theory and application to non-spherical stars, mnras 181 (1977) 375–389.

[3]. Lucy L, A numerical approach to the testing of the fission hypothesis, aj 82 (1977) 1013–1024.

[4]. Bian X, Litvinov S, Qian R, Ellero M, Adams NA, Multiscale modeling of particle in suspension with smoothed dissipative particle dynamics, Physics of Fluids 24 (2012) 012002.

[5]. Vázquez-Quesada A, Bian X, Ellero M, Three-dimensional simulations of dilute and concentrated suspensions using smoothed particle hydrodynamics, Computational Particle Mechanics 3 (2016) 167–178.

[6]. Lei H, Mundy CJ, Schenter GK, Voulgarakis NK, Modeling nanoscale hydrodynamics by smoothed dissipative particle dynamics, The Journal of Chemical Physics 142 (2015) 194504. [PubMed: 26001466]

[7]. Moreno N, Vignal P, Li J, Calo VM, Multiscale modeling of blood flow: Coupling finite elements with smoothed dissipative particle dynamics, Procedia Computer Science 18 (2013) 2565–2574. 2013 International Conference on Computational Science.

[8]. Müller K, Fedosov DA, Gompper G, Margination of micro- and nano-particles in blood flow and its effect on drug delivery, Nature Scientific Reports 4 (2014). Article.

[9]. Lei H, Baker NA, Wu L, Schenter GK, Mundy CJ, Tartakovsky AM, Smoothed dissipative particle dynamics model for mesoscopic multiphase flows in the presence of thermal fluctuations, Phys. Rev. E 94 (2016) 023304. [PubMed: 27627409]

[10]. Litvinov S, Xie Q, Hu X, Adams N, Ellero M, Simulation of individual polymer chains and polymer solutions with smoothed dissipative particle dynamics, Fluids 1 (2016).

[11]. Ye T, Phan-Thien N, Lim CT, Peng L, Shi H, Hybrid smoothed dissipative particle dynamics and immersed boundary method for simulation of red blood cells in flows, Phys. Rev. E 95 (2017) 063314. [PubMed: 28709282]

[12]. Adami S, Hu X, Adams N, A transport-velocity formulation for smoothed particle hydrodynamics, Journal of Computational Physics 241 (2013) 292–307.

[13]. Xu X, Deng X-L, An improved weakly compressible SPH method for simulating free surface flows of viscous and viscoelastic fluids, Computer Physics Communications 201 (2016) 43–62.

[14]. Hieber S, Koumoutsakos P, An immersed boundary method for smoothed particle hydrodynamics of self-propelled swimmers, Journal of Computational Physics 227 (2008) 8636–8654.

[15]. Vacondio R, Rogers B, Stansby PK, Mignosa P, Feldman J, Variable resolution for sph: a dynamic particle coalescing and splitting scheme, Computer Methods in Applied Mechanics and Engineering 256 (2013) 132–148.

[16]. Barcarolo DA, Le Touzé D, Oger G, De Vuyst F, Adaptive particle refinement and derefinement applied to the smoothed particle hydrodynamics method, Journal of Computational Physics 273 (2014) 640–657.

[17]. Vacondio R, Rogers B, Stansby PK, Mignosa P, Variable resolution for sph in three dimensions: Towards optimal splitting and coalescing for dynamic adaptivity, Computer Methods in Applied Mechanics and Engineering 300 (2016) 442–460.

[18]. Ji Z, Fu L, Hu XY, Adams NA, A new multi-resolution parallel framework for SPH, Computer Methods in Applied Mechanics and Engineering 346 (2019) 1156–1178.

[19]. Zhang C, Rezavand M, Hu X, A multi-resolution SPH method for fluid-structure interactions, Journal of Computational Physics (2020) 110028.

[20]. Colagrossi A, Landrini M, Numerical simulation of interfacial flows by smoothed particle hydrodynamics, Journal of computational physics 191 (2003) 448–475.

[21]. Feldman J, Bonet J, Dynamic refinement and boundary contact forces in SPH with applications in fluid flow problems, International Journal for Numerical Methods in Engineering 72 (2007) 295–324.

[22]. Adami S, Hu X, Adams N, A generalized wall boundary condition for smoothed particle hydrodynamics, Journal of Computational Physics 231 (2012) 7057–7075.

[23]. Monaghan J, Kajtar J, SPH particle boundary forces for arbitrary boundaries, Computer Physics Communications 180 (2009) 1811–1820.

[24]. Macia F, Antuono M, González LM, Colagrossi A, Theoretical analysis of the no-slip boundary condition enforcement in SPH methods, Progress of theoretical physics 125 (2011) 1091–1121.

[25]. Ferrand M, Laurence DR, Rogers BD, Violeau D, Kassiotis C, Unified semi-analytical wall boundary conditions for inviscid, laminar or turbulent flows in the meshless SPH method, International Journal for Numerical Methods in Fluids 71 (2012) 446–472.

[26]. Colagrossi A, Bouscasse B, Antuono M, Marrone S, Particle packing algorithm for SPH schemes, Computer Physics Communications 183 (2012) 1641–1653.

[27]. Ferrand M, Laurence D, Rogers BD, Violeau D, Kassiotis C, Unified semi-analytical wall boundary conditions for inviscid, laminar or turbulent flows in the meshless SPH method, International Journal for Numerical Methods in Fluids 71 (2013) 446–472.

[28]. Bierbrauer F, Bollada PC, Phillips TN, A consistent reflected image particle approach to the treatment of boundary conditions in smoothed particle hydrodynamics, Computer Methods in Applied Mechanics and Engineering 198 (2009) 3400–3410.

[29]. Amicarelli A, Agate G, Guandalini R, A 3d fully lagrangian smoothed particle hydrodynamics model with both volume and surface discrete elements, International journal for numerical methods in engineering 95 (2013) 419–450.

[30]. Colagrossi A, Antuono M, Souto-Iglesias A, Le Touzé D, Theoretical analysis and numerical verification of the consistency of viscous smoothed-particle-hydrodynamics formulations in simulating free-surface flows, Physical Review E 84 (2011) 026705.

[31]. Spheric-SPH grand challenges, 2020. URL: https://spheric-sph.org/grand-challenges.

[32]. Valizadeh A, Monaghan JJ, A study of solid wall models for weakly compressible SPH, Journal of Computational Physics 300 (2015) 5–19.

[33]. Federico I, Marrone S, Colagrossi A, Aristodemo F, Antuono M, Simulating 2d open-channel flows through an SPH model, European Journal of Mechanics - B/Fluids 34 (2012) 35–46.

[34]. Peskin CS, The immersed boundary method, Acta Numerica 11 (2002) 479–517.

[35]. Khayyer A, Gotoh H, Falahaty H, Shimizu Y, An enhanced ISPH–SPH coupled method for simulation of incompressible fluid–elastic structure interactions, Computer Physics Communications 232 (2018) 139–164.

[36]. Zhan L, Peng C, Zhang B, Wu W, A stabilized TL-WC SPH approach with GPU acceleration for threedimensional fluid–structure interaction, Journal of Fluids and Structures 86 (2019) 329–353.

[37]. Li Z, Bian X, Tang Y-H, Karniadakis GE, A dissipative particle dynamics method for arbitrarily complex geometries, Journal of Computational Physics 355 (2018) 534–547.

[38]. Irgens F, Continuum Mechanics, Springer Berlin Heidelberg, 2008.

[39]. Nestor R, Basa M, Quinlan N, Moving boundary problems in the finite volume particle method, in: 3rd ERCOFTAC SPHERIC workshop on SPH applications, Switzerland, Lausanne, 2008.

[40]. Shadloo MS, Zainali A, Yildiz M, Suleman A, A robust weakly compressible sph method and its comparison with an incompressible SPH, International Journal for Numerical Methods in Engineering 89 (2012) 939–956.

[41]. Lind S, Xu R, Stansby P, Rogers B, Incompressible smoothed particle hydrodynamics for free-surface flows: A generalised diffusion-based algorithm for stability and validations for impulsive flows and propagating waves, Journal of Computational Physics 231 (2012) 1499–1523.

[42]. Khayyer A, Gotoh H, Shimizu Y, Comparative study on accuracy and conservation properties of two particle regularization schemes and proposal of an optimized particle shifting scheme in ISPH context, Journal of Computational Physics 332 (2017) 236–256.

[43]. Oger G, Marrone S, Touzé DL, de Leffe M, SPH accuracy improvement through the combination of a quasi-lagrangian shifting transport velocity and consistent ale formalisms, Journal of Computational Physics 313 (2016) 76–98.

[44]. Monaghan J, SPH without a tensile instability, Journal of Computational Physics 159 (2000) 290–311.

[45]. Zhang C, Hu XY, Adams NA, A generalized transport-velocity formulation for smoothed particle hydrodynamics, Journal of Computational Physics 337 (2017) 216–232.

[46]. Litvinov S, Hu X, Adams N, Towards consistence and convergence of conservative SPH approximations, Journal of Computational Physics 301 (2015) 394–401.

[47]. Morris JP, Fox PJ, Zhu Y, Modeling low reynolds number incompressible flows using SPH, Journal of Computational Physics 136 (1997) 214–226.

[48]. Monaghan JJ, Lattanzio JC, A Refined Method for Astrophysical Problems, Astronomy and Astrophysics 149 (1985) 135–143.

[49]. Monaghan JJ, Smoothed particle hydrodynamics, Annual Review of Astronomy and Astrophysics 30 (1992) 543–574.

[50]. Inutsuka S.-i., Reformulation of smoothed particle hydrodynamics with Riemann solver, Journal of Computational Physics 179 (2002) 238–267.

[51]. Murante G, Borgani S, Brunino R, Cha S-H, Hydrodynamic simulations with the godunov smoothed particle hydrodynamics, Monthly Notices of the Royal Astronomical Society 417 (2011) 136–153.

[52]. Puri K, Ramachandran P, Approximate Riemann solvers for the Godunov SPH (GSPH), Journal of Computational Physics 270 (2014) 432–458.

[53]. Shao S, Lo EY, Incompressible SPH method for simulating newtonian and non-newtonian flows with a free surface, Advances in Water Resources 26 (2003) 787–800.

[54]. Ellero M, Serrano M, Español P, Incompressible smoothed particle hydrodynamics, Journal of Computational Physics 226 (2007) 1731–1752.

[55]. Vázquez-Quesada A, Ellero M, Español P, Consistent scaling of thermal fluctuations in smoothed dissipative particle dynamics, The Journal of Chemical Physics 130 (2009) 034901. [PubMed: 19173537]

[56]. Gray J, Monaghan J, Swift R, SPH elastic dynamics, Computer Methods in Applied Mechanics and Engineering 190 (2001) 6641–6662.

[57]. Colagrossi A, Landrini M, Numerical simulation of interfacial flows by smoothed particle hydrodynamics, Journal of Computational Physics 191 (2003) 448–475. P.

[58]. Sun P, Colagrossi A, Marrone S, Antuono M, Zhang A, Multi-resolution delta-plus-SPH with tensile instability control: Towards high reynolds number flows, Computer Physics Communications 224 (2018) 63–80.

[59]. Shepard D, A two-dimensional interpolation function for irregularly-spaced data, in: Proceedings of the 1968 23rd ACM national conference, ACM, 1968, pp. 517–524.

[60]. Molteni D, Colagrossi A, A simple procedure to improve the pressure evaluation in hydrodynamic context using the SPH, Computer Physics Communications 180 (2009) 861–872.

[61]. Lifshitz EM, Pitaevskii L, Berestetskii V, Landau and lifshitz course of theoretical physics, Statistical physics 5 (1980).

[62]. Plimpton S, Fast parallel algorithms for short-range molecular dynamics, Journal of Computational Physics 117 (1995) 1–19.

[63]. Ferrand M, Laurence DR, Rogers BD, Violeau D, Kassiotis C, Unified semi-analytical wall boundary conditions for inviscid, laminar or turbulent flows in the meshless SPH method, International Journal for Numerical Methods in Fluids 71 (2013) 446–472.

[64]. Wendland H, Piecewise polynomial, positive definite and compactly supported radial functions of minimal degree, Advances in computational Mathematics 4 (1995) 389–396.

[65]. Ferziger JH, Perić M, Computational methods for fluid dynamics, volume 3, Springer, 2002.

[66]. Ghia U, Ghia K, Shin C, High-re solutions for incompressible flow using the navier-stokes equations and a multigrid method, Journal of Computational Physics 48 (1982) 387–411.

[67]. Gray DD, Giorgini A, The validity of the boussinesq approximation for liquids and gases, International Journal of Heat and Mass Transfer 19 (1976) 545–551.

[68]. Moukalled F, Acharya S, Natural convection in the annulus between concentric horizontal circular and square cylinders, Journal of Thermophysics and Heat Transfer 10 (1996) 524–531.

[69]. Shu C, Zhu YD, Efficient computation of natural convection in a concentric annulus between an outer square cylinder and an inner circular cylinder, International Journal for Numerical Methods in Fluids 38 (2002) 429–445.

[70]. Peng Y, Chew YT, Shu C, Numerical simulation of natural convection in a concentric annulus between a square outer cylinder and a circular inner cylinder using the taylor-series-expansion and least-squares-based lattice boltzmann method, Phys. Rev. E 67 (2003) 026701.

[71]. Angeli D, Levoni P, Barozzi GS, Numerical predictions for stable buoyant regimes within a square cavity containing a heated horizontal cylinder, International Journal of Heat and Mass Transfer 51 (2008) 553–565.

[72]. De AK, Dalal A, A numerical study of natural convection around a square, horizontal, heated cylinder placed in an enclosure, International Journal of Heat and Mass Transfer 49 (2006) 4608–4623.

[73]. Butler C, Newport D, Geron M, Natural convection experiments on a heated horizontal cylinder in a differentially heated square cavity, Experimental Thermal and Fluid Science 44 (2013) 199–208.

[74]. Cesini G, Paroncini M, Cortella G, Manzan M, Natural convection from a horizontal cylinder in a rectangular cavity, International Journal of Heat and Mass Transfer 42 (1999) 1801–1811.

[75]. Israeli M, Orszag SA, Approximation of radiation boundary conditions, Journal of Computational Physics 41 (1981) 115–135.

[76]. Drawert B, Jacob B, Li Z, Yi T-M, Petzold L, Validation data for a hybrid smoothed dissipative particle dynamics (SDPD) spatial stochastic simulation algorithm (sSSA) method, Data in Brief 22 (2019) 11–15. [PubMed: 30581900]

[77]. Van Liedekerke P, Ghysels P, Tijskens E, Samaey G, Smeedts B, Roose D, Ramon H, A particle-based model to simulate the micromechanics of single-plant parenchyma cells and aggregates, Physical biology 7 (2010) 026006. [PubMed: 20505228]

[78]. Van Liedekerke P, Tijskens E, Ramon H, Ghysels P, Samaey G, Roose D, Particle-based model to simulate the micromechanics of biological cells, Physical Review E 81 (2010) 061906.

[79]. Alvaro CG, Thorner J, Heterotrimeric G Protein-coupled Receptor Signaling in Yeast Mating Pheromone Response, The Journal of Biological Chemistry 291 (2016) 7788–7795. [PubMed: 26907689]

[80]. Levin DE, Regulation of cell wall biogenesis in Saccharomyces cerevisiae: the cell wall integrity signaling pathway, Genetics 189 (2011) 1145–1175. [PubMed: 22174182]

[81]. Banavar SP, Gomez C, Trogdon M, Petzold LR, Yi T-M, Campàs O, Mechanical feedback coordinates cell wall expansion and assembly in yeast mating morphogenesis, PLoS computational biology 14 (2018) e1005940. [PubMed: 29346368]

[82]. Moore TI, Tanaka H, Kim HJ, Jeon NL, Yi TM, Yeast G-proteins mediate directional sensing and polarization behaviors in response to changes in pheromone gradient direction, Molecular Biology of the Cell 24 (2013) 521–534. [PubMed: 23242998]

[83]. McClure AW, Minakova M, Dyer JM, Zyla TR, Elston TC, Lew DJ, Role of Polarized G Protein Signaling in Tracking Pheromone Gradients, Developmental Cell 35 (2015) 471–482. [PubMed: 26609960]

[84]. Errede B, Vered L, Ford E, Pena MI, Elston TC, Pheromone-induced morphogenesis and gradient tracking are dependent on the MAPK Fus3 binding to Ga, Molecular Biology of the Cell 26 (2015) 3343–3358. [PubMed: 26179918]

[85]. Renardy M, Yi T-M, Xiu D, Chou C-S, Parameter uncertainty quantification using surrogate models applied to a spatial model of yeast mating polarization, PLoS computational biology 14 (2018) e1006181.

[86]. Trogdon M, Drawert B, Gomez C, Banavar SP, Yi T-M, Campàs O, Petzold LR, The effect of cell geometry on polarization in budding yeast, PLoS Computational Biology 14 (2018).

[87]. Lawson MJ, Drawert B, Khammash M, Petzold L, Yi T-M, Spatial Stochastic Dynamics Enable Robust Cell Polarization, PLoS Computational Biology 9 (2013).

[88]. Barnhart E, Lee K-C, Allen GM, Theriot JA, Mogilner A, Balance between cell-substrate adhesion and myosin contraction determines the frequency of motility initiation in fish keratocytes, Proceedings of the National Academy of Sciences 112 (2015) 5045–5050.

[89]. Hu J, Jafari S, Han Y, Grodzinsky AJ, Cai S, Guo M, Size- and speed-dependent mechanical behavior in living mammalian cytoplasm, Proceedings of the National Academy of Sciences 114 (2017) 9529–9534.

[90]. Barfield RM, Fromme JC, Schekman R, The exomer coat complex transports Fus1p to the plasma membrane via a novel plasma membrane sorting signal in yeast, Molecular Biology of the Cell 20 (2009) 4985–4996. [PubMed: 19812245]

[91]. Fu L, Ji Z, An optimal particle setup method with Centroidal Voronoi Particle dynamics, Computer Physics Communications 234 (2019) 72–92.

[92]. Nasar A, Rogers BD, Revell A, Stansby P, Flexible slender body fluid interaction: vector-based discrete element method with Eulerian smoothed particle hydrodynamics, Computers & Fluids 179 (2019) 563–578.

[93]. Nasar A, Rogers BD, Revell A, Stansby P, Lind S, Eulerian weakly compressible smoothed particle hydrodynamics (sph) with the immersed boundary method for thin slender bodies, Journal of Fluids and Structures 84 (2019) 263–282.

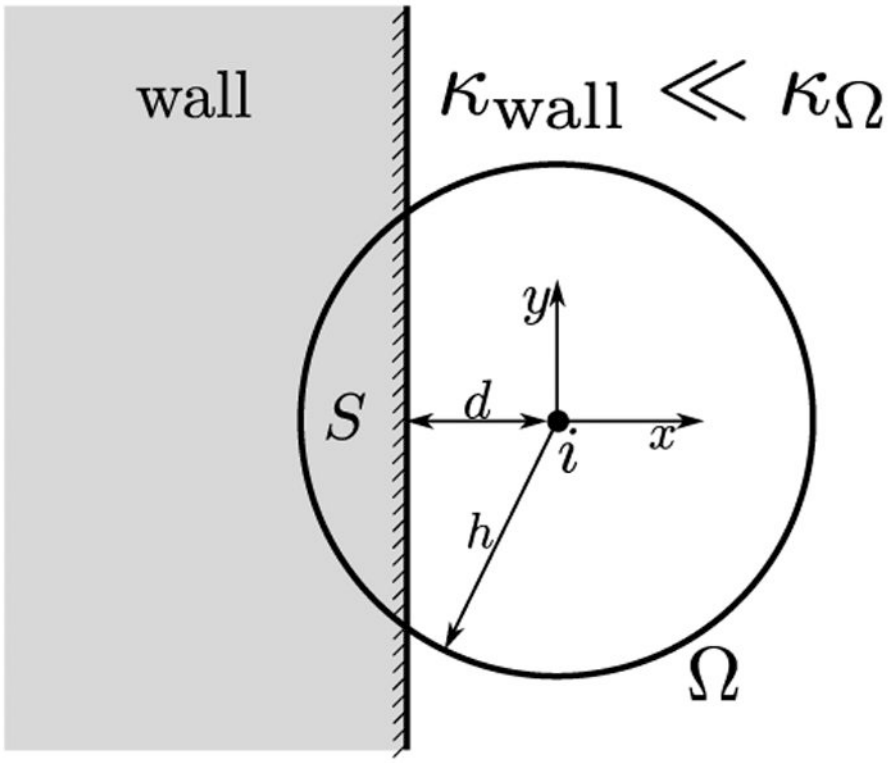

Fig. 1.
Schematic showing the influence domain Ω around particle *i*, nearby wall and intersection between Ω and the wall, denoted by *S*.

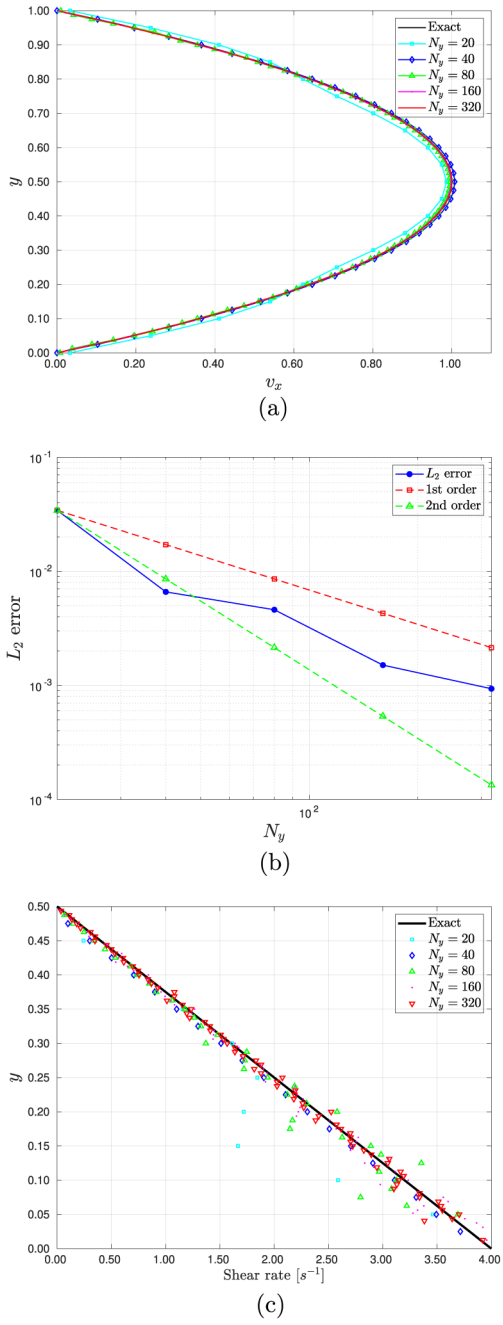

Fig. 2.

Results the SPH-BVF method and using Lucy kernel: (a) Streamwise profiles of a fully-developed, steady-state Poiseuille flow in a periodic channel, for N_y = 20, 40, 80, 160 and 320 particles in the cross-stream direction. (b) Convergence graph showing the L_2 error versus the refinement. (c) Comparison of shear rate in the lower part ($0 \leq y \leq 0.5$) of the channel.

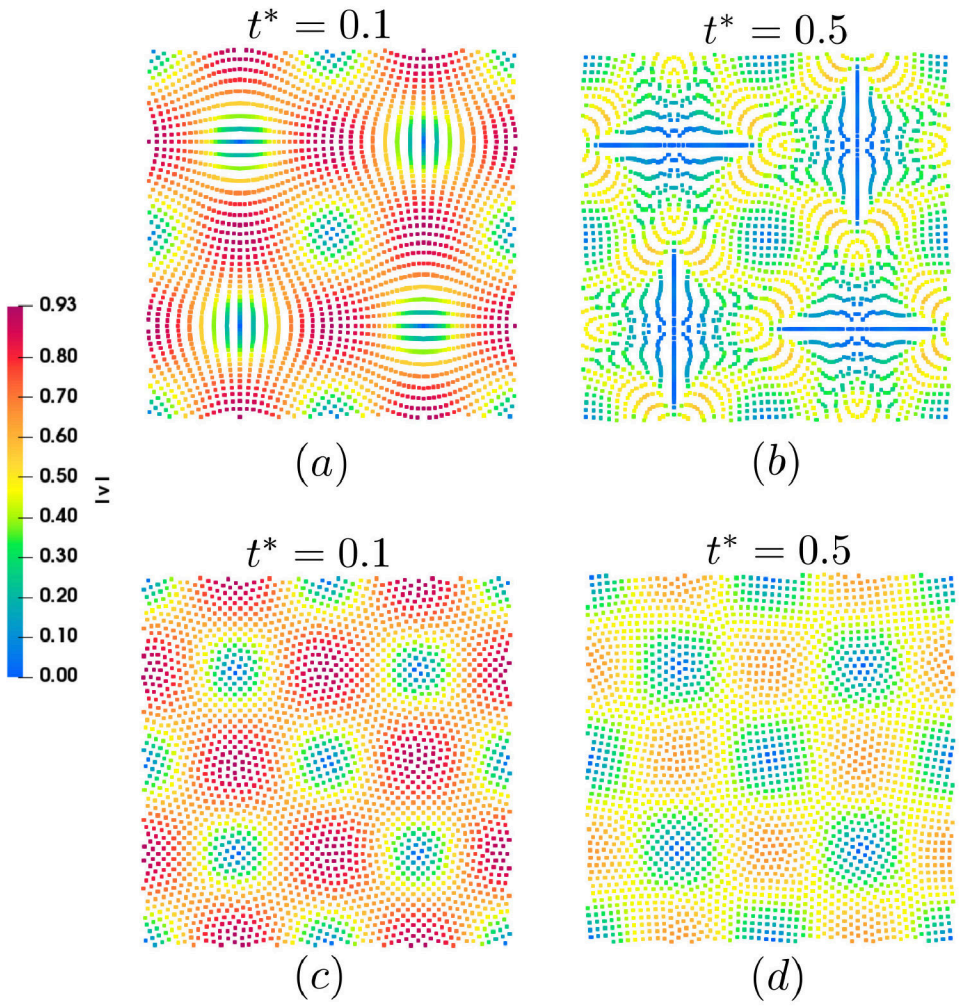

Fig. 3.

Contour plots of the norm of the velocity vector showing particle arrangements in 2D Taylor-Green vortex simulations at two time points: (a) Standard SPH, t^* = 0.1, (b) Standard SPH, t^* = 0.5, (c) SPH-BVF (present method), t^* = 0.1, (d) SPH-BVF (present method), t^* = 0.5.

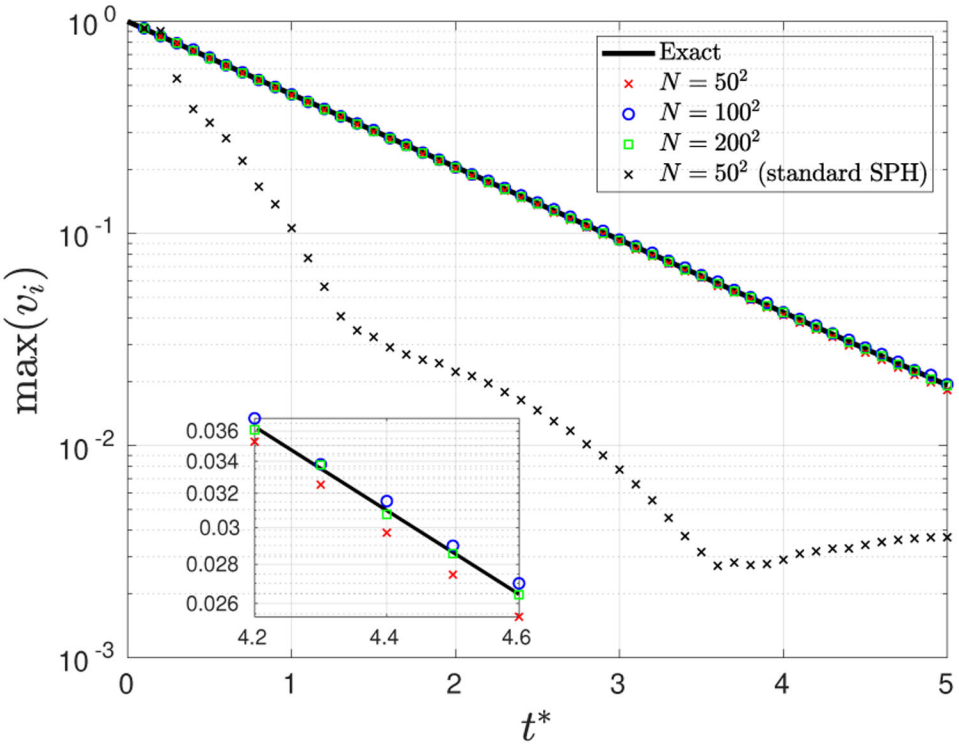

Fig. 4.

Temporal evolution of the decay of the maximum velocity (semi-log scale) in 2D Taylor-Green vortex simulations for three particle refinements (*N*) that are compared to the exact analytical solution and standard SPH. Inset shows an expanded view of a section of the graph.

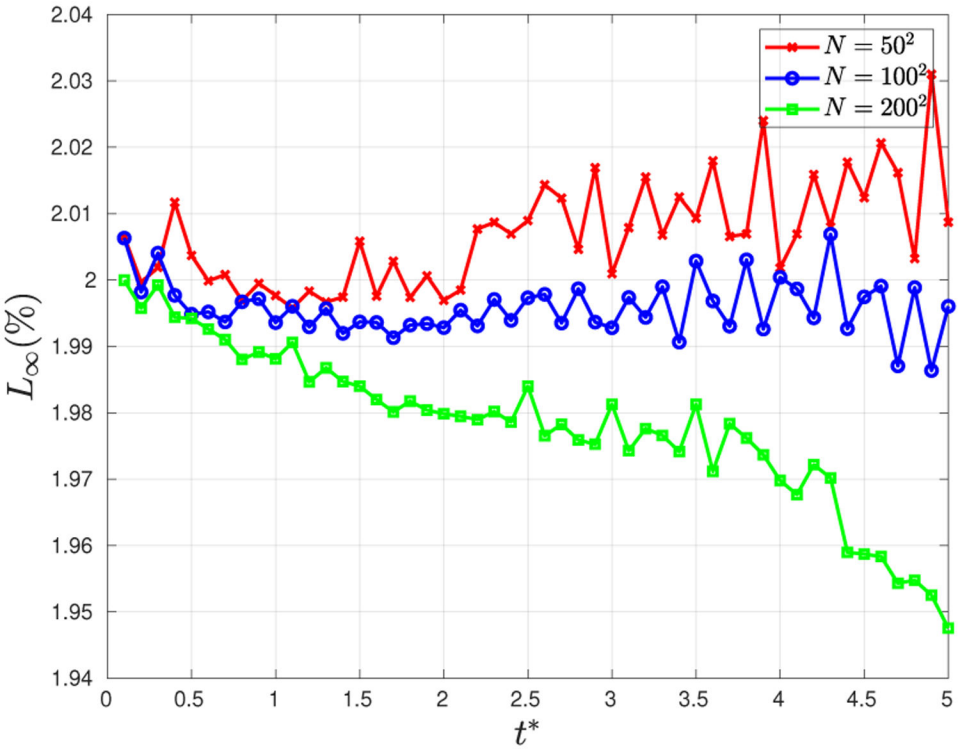

Fig. 5.

Temporal evolution of the relative error of the maximum velocity (L_∞ norm) in the Taylor-Green simulations for three particle refinements (N).

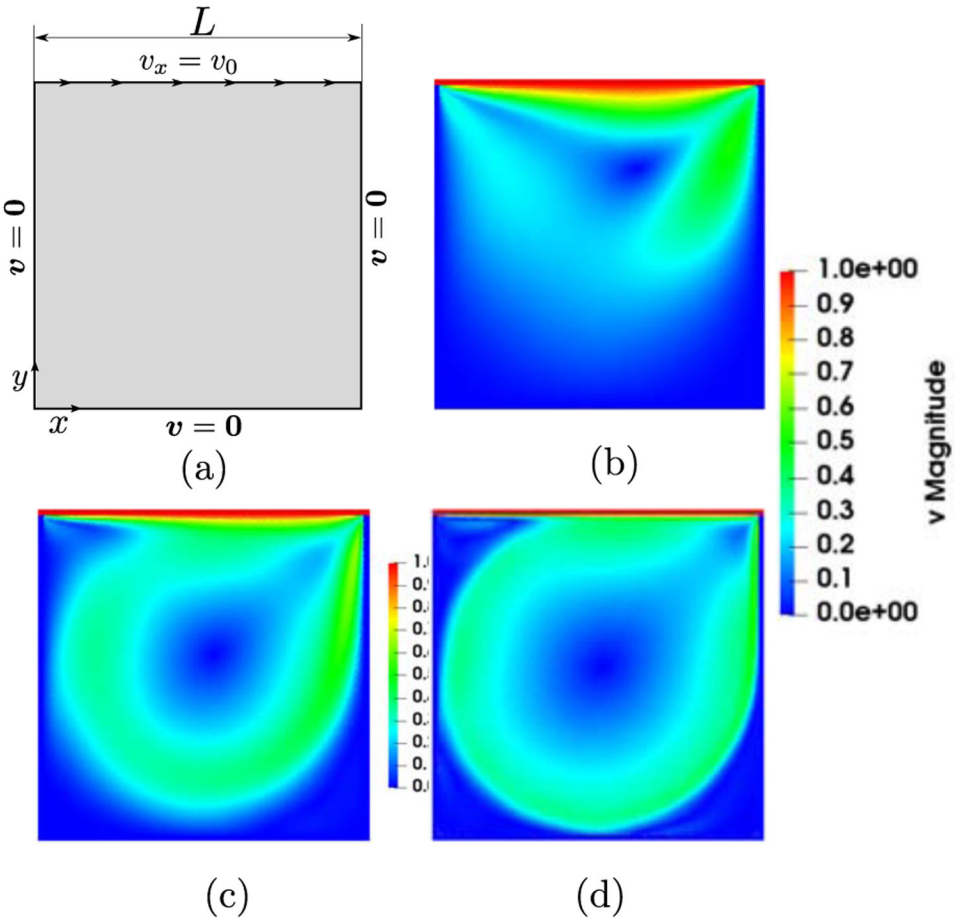

Fig. 6.

(a) Schematic of lid-driven cavity flow. Isocontours of velocity magnitude for (b) *Re* = 100, (c) *Re* = 1000 and (d) *Re* = 10000 at steady-state.

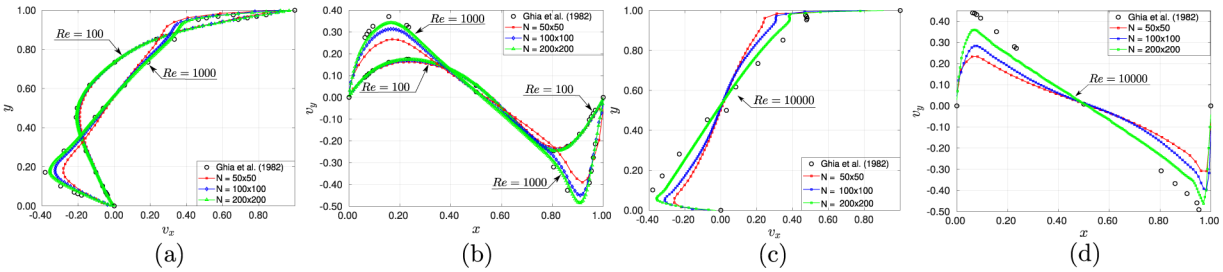

Fig. 7.

(a), (c) Vertical and (b), (d) horizontal velocity profiles for $Re = 100$, $Re = 1000$ and $Re = 10000$ compared with the reference results of Ghia et al. [66].

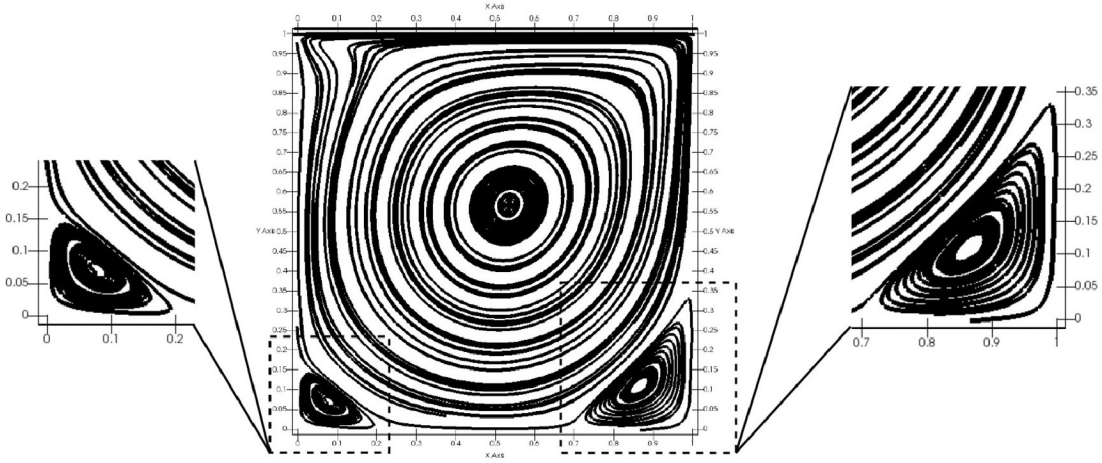

Fig. 8.

Streamlines and patterns of the corner vortices in the cavity for $Re = 1000$, obtained with the SPH-BVF method.

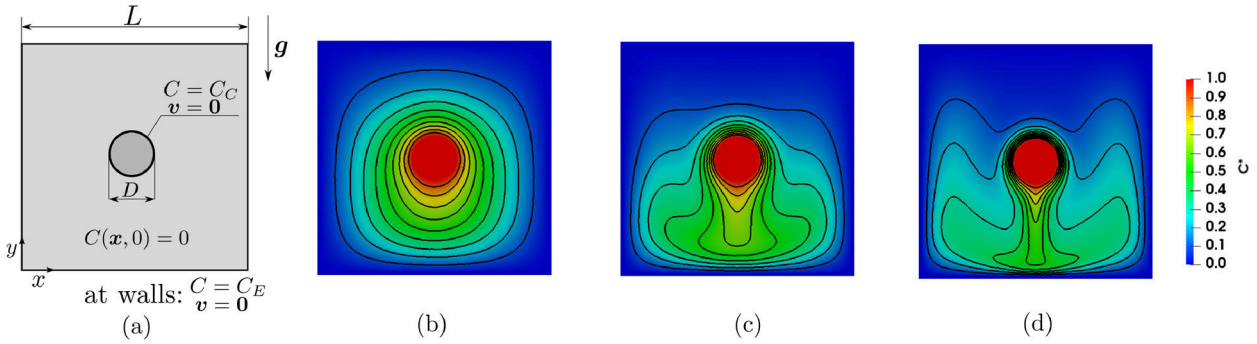

Fig. 9.

(a) Schematic of natural convection in a cylinder inside a square enclosure. (b) Isocontours of the dimensionless concentration field C for $Ra = 10^4$, (c) $Ra = 10^5$ and (d) $Ra = 10^6$ at steady-state.

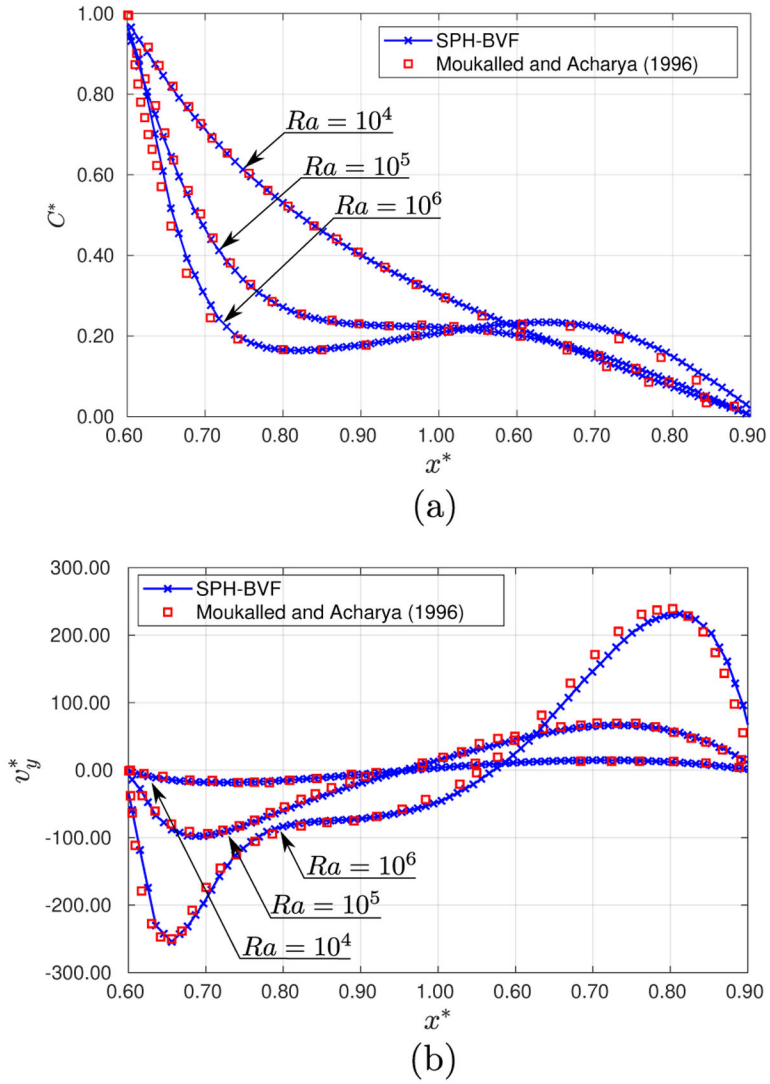

Fig. 10.

(a) Profiles of dimensionless concentration C^* and (b) y-velocity v_y^* profiles along the horizontal centerline of the cavity, for $Ra = 10^4$, 10^5 and 10^6, at steady-state.

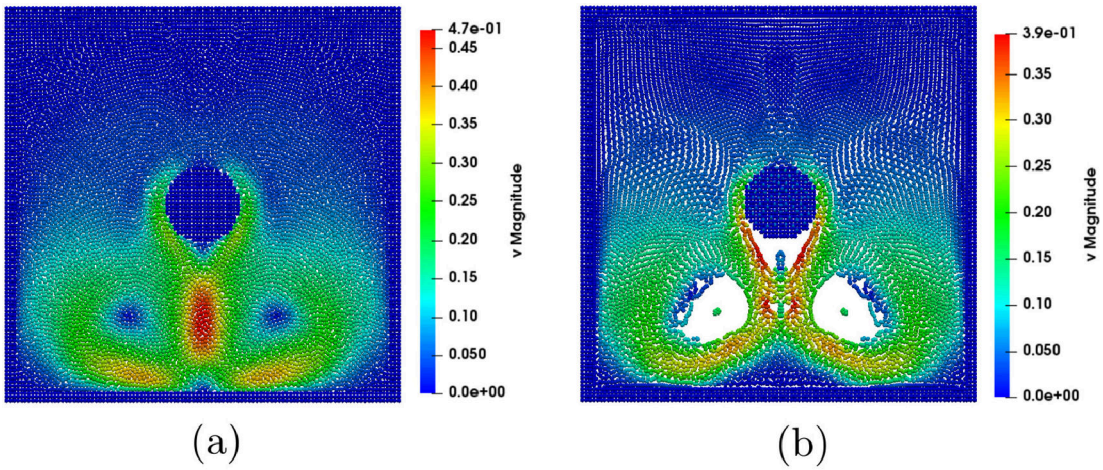

Fig. 11.

Comparison of mean velocity fields at time $t^* = 4$, for the natural convection problem solved using (a) SPH-BVF method and (b) standard SPH [2] method, showing that the proposed method prevents particle penetration and mitigates tensile instability and anisotropic particle alignment.

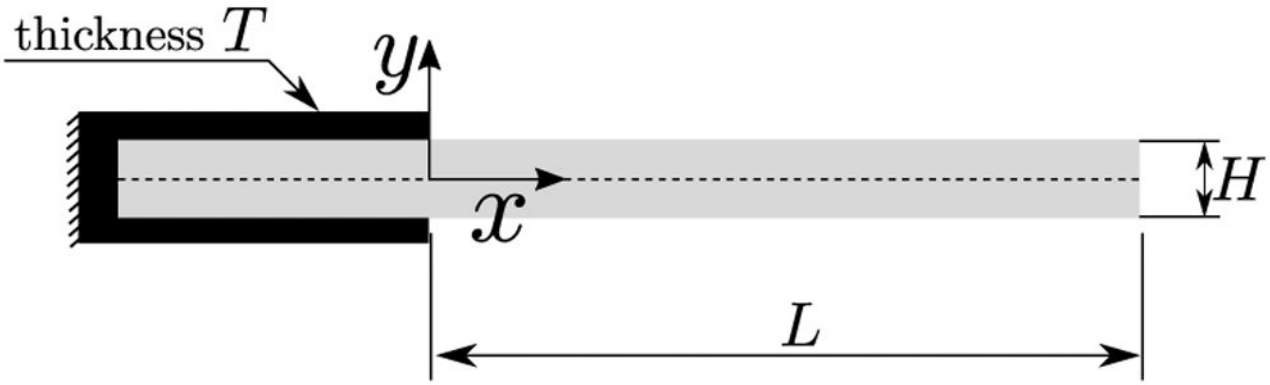

Fig. 12.
Schematic of the oscillating cantilever beam. The beam, initially at rest, is subject to the initial condition given by Eq. (70).

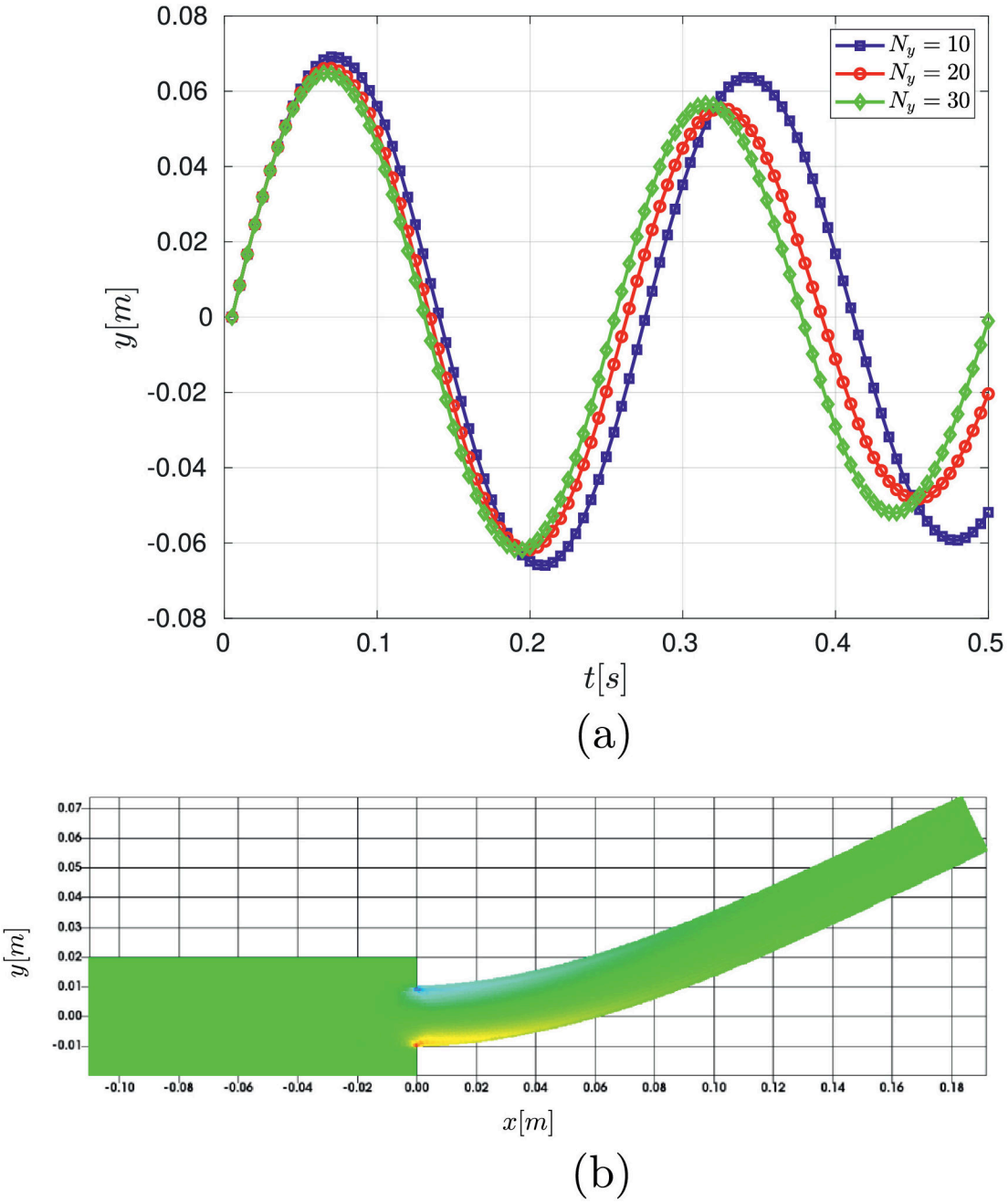

Fig. 13.

(a) Plots of the position of the centerline point at the tip of the beam ($y = 0$, $x = L$) for the case of $V_0 = 3 \times 10^{-2}$, illustrating the convergence of the SPH solid mechanics formulation. (b) Contour plots of total stress field σ_{xx} at $t = 0.07[s]$, for the case of $V_0 = 3 \times 10^{-2}$ and $N_y = 30$.

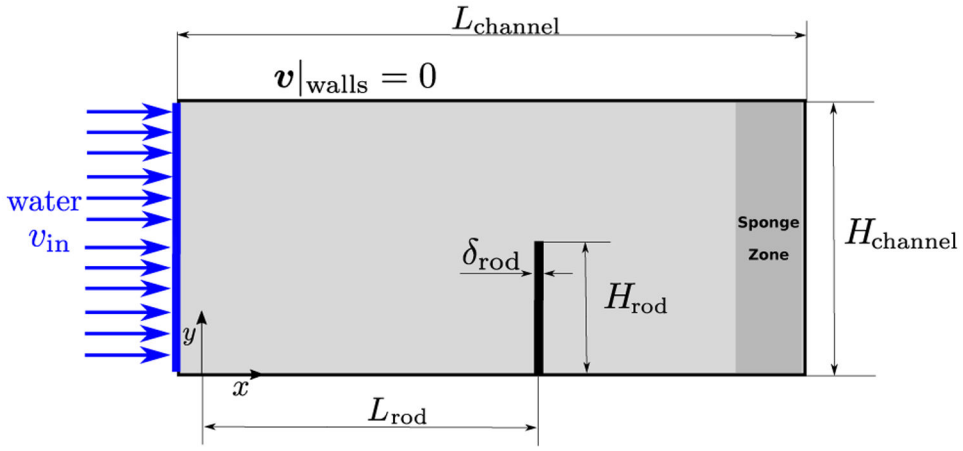

Fig. 14.

Schematic of the FSI problem. Water enters in a 2D microchannel, filled with water at rest, with uniform velocity v_{in}. An elastic rod located at the middle of the channel and fixed at the lower wall, constraints the fluid flow, causing a deformation in the rod.

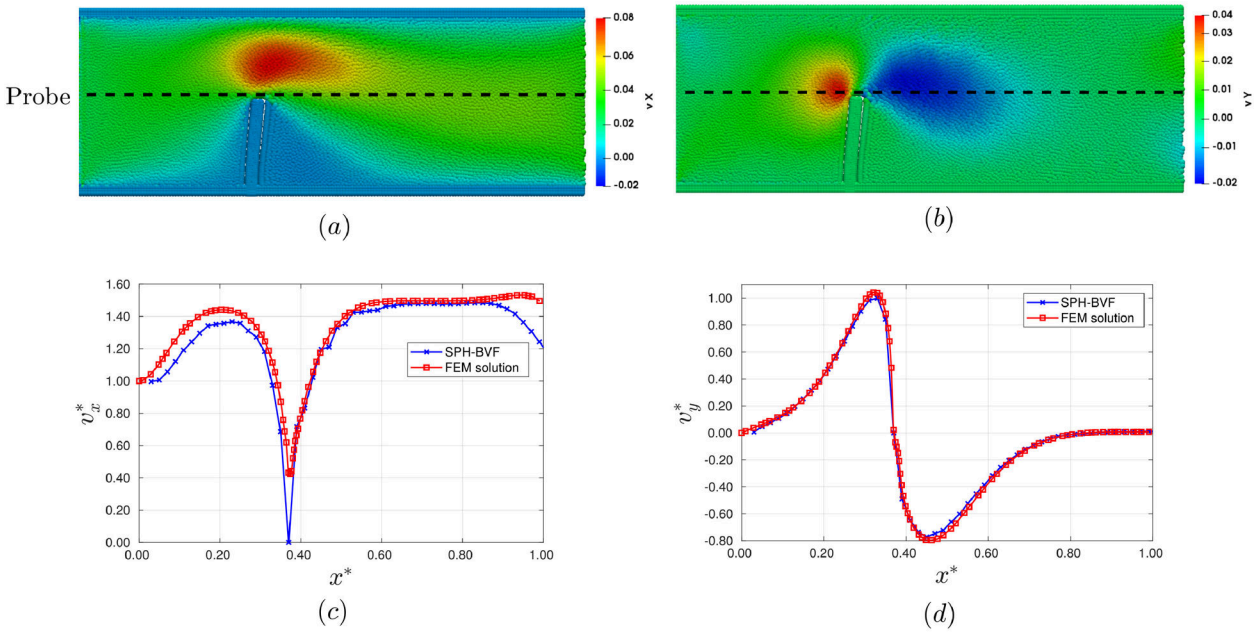

Fig. 15.

Top: contour plots of the (a) streamwise v_x and (b) cross-stream v_y velocity fields at steady-state. The beam has deformed slightly to the right. Bottom: comparison of dimensionless velocity profiles (c) v_x^* and (d) v_y^* for a probe located at the y-centerline of the channel, as depicted in the velocity profiles. Variables were rendered dimensionless for scaling purposes, as $v_x^* = v_x / v_{\text{in}}$ and $x^* = x/L_{\text{channel}}$.

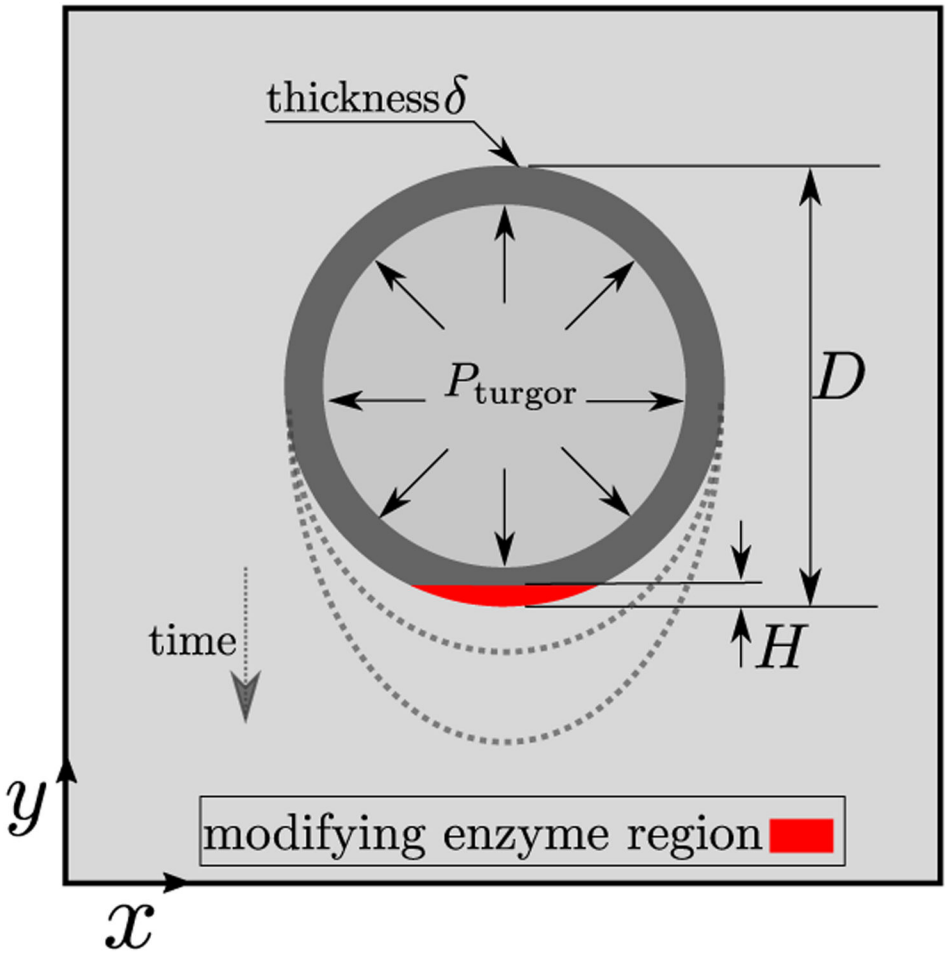

Fig. 16.

Schematic of yeast cell projection growth model. Cell wall modifying enzymes localized to region in red cause the softening of the cell wall. The internal turgor pressure pushes and deforms the cell wall at this weakened section, creating a mating projection. D is the diameter of the cell, H is the height of the enzyme region, and δ is the thickness of the cell wall.

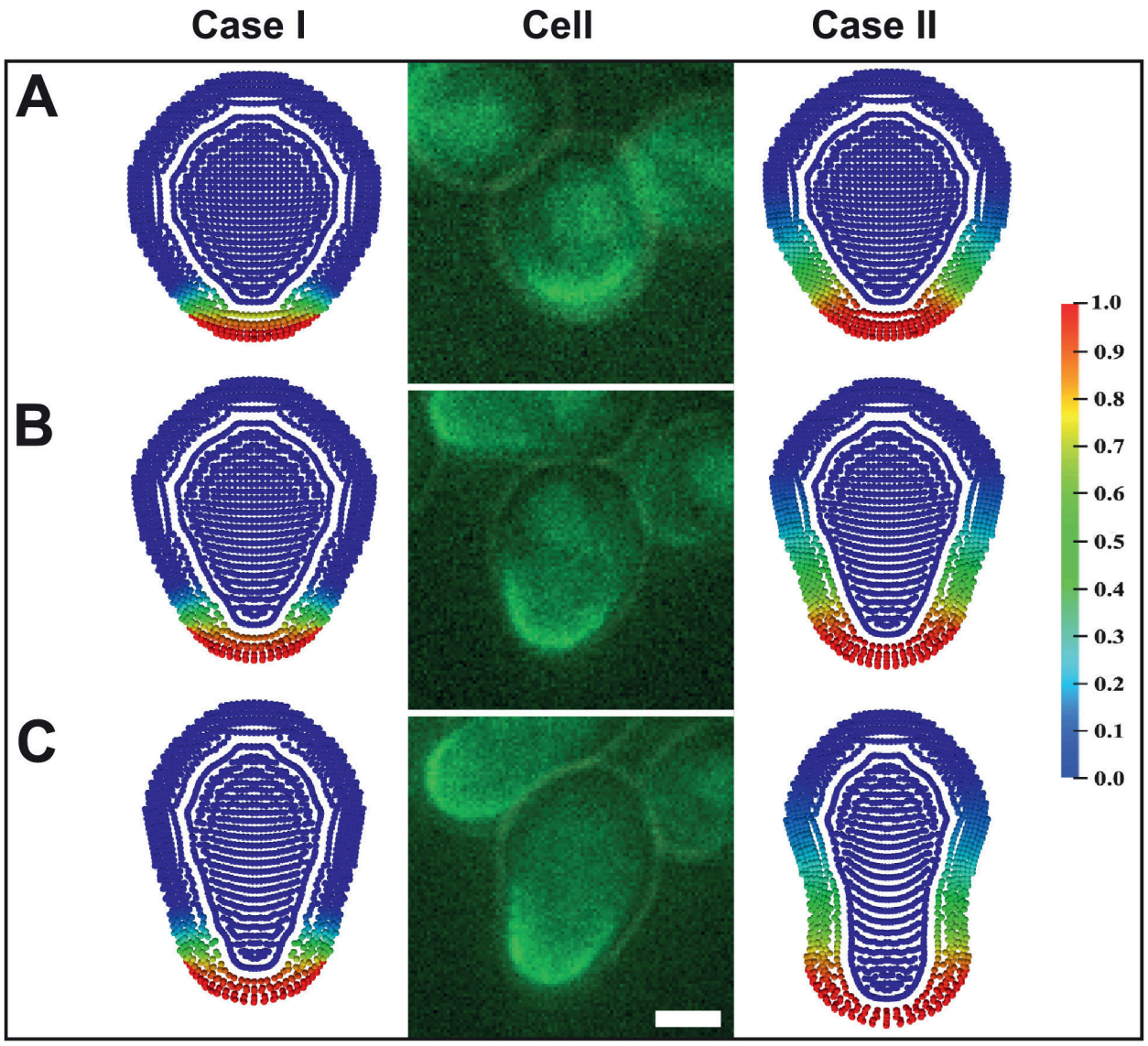

Fig. 17.

Simulations and experiments showing yeast mating projection growth over time. Cases I (left column, $\kappa_c = 10^{-13}$ [m^2/s]), II (right column, $\kappa_c = 10^{-12}$ [m^2/s]), and microscopy images of a *spa2*Δ cell responding to 1 μM mating pheromone α-factor (central column). Particles are colored by the concentration c of wall-modifying enzymes. Rows A, B and C indicate times of 2000, 3000 and 4000 seconds, respectively, for the simulations, and 30, 60, and 90 minutes for the experiments. Cells contain the secretion marker protein Fus1-GFP (green) to indicate where wall-modifying enzymes are transported. A broad tip protrudes from both simulations and experiments. Despite high internal turgor pressure and deformation, SPH-BVF is able to model the deforming boundaries without particle penetration or tension instability. Scale bar = 2 μm.

Table 1

Estimated errors and convergence rate of Poiseuille flow for different kernels.

Kernel	N_y	L_2 Error[a]	Converg. rate, p[630]
Lucy	20	3.425×10^{-2}	-
Lucy	40	6.598×10^{-3}	2.376
Lucy	80	4.601×10^{-3}	0.520
Lucy	160	1.505×10^{-3}	1.612
Lucy	320	9.340×10^{-4}	0.688
Cubic spline	20	2.169×10^{-2}	-
Cubic spline	40	1.690×10^{-2}	0.360
Cubic spline	80	9.512×10^{-3}	0.828
Cubic spline	160	5.786×10^{-3}	0.718
Cubic spline	320	6.620×10^{-4}	−0.194
Wendland quintic	20	3.153×10^{-2}	-
Wendland quintic	40	2.864×10^{-2}	0.138
Wendland quintic	80	7.022×10^{-3}	2.028
Wendland quintic	160	1.408×10^{-2}	−1.003
Wendland quintic	320	1.206×10^{-2}	0.223

[a]Error computed at steady-state, $t = 100$.

Table 2

Relative errors for oscillating cantilever beam for various velocity amplitudes V_0 and particle refinements.

V_0	Δ_p	N_y	First period (present work)	First period (analytical[a])	Relative error (%)
$1\times10^{-3}[m/s]$	0.2/10[m]	10	$2.747\times10^{-1}[s]$	$2.540\times10^{-1}[s]$	8.150
$1\times10^{-3}[m/s]$	0.2/20[m]	20	$2.605\times10^{-1}[s]$	$2.540\times10^{-1}[s]$	2.559
$1\times10^{-3}[m/s]$	0.2/30[m]	30	$2.539\times10^{-1}[s]$	$2.540\times10^{-1}[s]$	−0.039
$1\times10^{-2}[m/s]$	0.2/10[m]	10	$2.757\times10^{-1}[s]$	$2.540\times10^{-1}[s]$	8.543
$1\times10^{-2}[m/s]$	0.2/20[m]	20	$2.618\times10^{-1}[s]$	$2.540\times10^{-1}[s]$	3.071
$1\times10^{-2}[m/s]$	0.2/30[m]	30	$2.546\times10^{-1}[s]$	$2.540\times10^{-1}[s]$	0.236
$3\times10^{-2}[m/s]$	0.2/10[m]	10	$2.756\times10^{-1}[s]$	$2.540\times10^{-1}[s]$	8.504
$3\times10^{-2}[m/s]$	0.2/20[m]	20	$2.635\times10^{-1}[s]$	$2.540\times10^{-1}[s]$	3.740
$3\times10^{-2}[m/s]$	0.2/20[m]	30	$2.556\times10^{-1}[s]$	$2.540\times10^{-1}[s]$	0.623

[a]Based on Zhang et al. [45], Lifshitz et al. [61]

Table 3

Physical parameters adopted in the FSI simulation.

Parameter	Value	Description
H_{channel}	100 [μm]	channel height
L_{channel}	300 [μm]	channel width
H_{rod}	50 [μm]	rod height
L_{rod}	100 [μm]	horizonta position (rod)
δ_{rod}	5 [μm]	rod thickness
E	2×10^5 [Pa]	Young modulus (rod)
ν_p	0.33	Poisson ratio (rod)
ρ_f	1000 [kg/m^3]	fluid density
ρ_{rod}	7850 [kg/m^3]	rod density
μ_f	10^{-3} [$Pa\ s$]	viscosity of fluid
v_{in}	3.33×10^{-2} [m/s]	inlet fluid velocity

Table 4

Physical parameters used in the cell polarization simulation.

Parameter	Value	Description
δ	2.5 [μm]	cell wall thickness
D	10 [μm]	diameter of the cell
H	1.25 [μm]	height of enzyme region
E	10^6 [Pa]	Young modulus of cell wall
G_0	3.58×10^5 [Pa]	reference shear modulus of cell wall
ν_p	0.3975	Poisson ratio of cell wall
K_f	5×10^5 [Pa]	bulk modulus of extracellular fluid
K_c	5×10^5 [Pa]	bulk modulus of cytoplasm
ρ_f	1000 [kg/m^3]	density of extracellular fluid
ρ_c	1500 [kg/m^3]	density of cytoplasm
ρ_w	1100 [kg/m^3]	density of cell wall
μ_f	10^{-3} [$Pa\,s$]	dynamic viscosity of fluid
μ_c	10^{-3} [$Pa\,s$]	dynamic viscosity of cytoplasm
R	0.99[m^3/mol]	rate of enzymatic softening

Table 5

Two cases simulated with parameter values and number of particles.

Case number	Mass diffusivity (κ_c)	Number of particles (N)
I	10^{-13} [m^2/s]	840 (wall), 716 (cytoplasm)
II	10^{-12} [m^2/s]	840 (wall), 716 (cytoplasm)